Applied Thermal Engineering 250 (2024) 123461

Contents lists available at ScienceDirect

Applied Thermal Engineering

journal homepage: www.elsevier.com/locate/ate

Research Paper

Thermo-electrochemical level-set topology optimization of a heat exchanger for lithium-ion batteries for electric vertical take-off and landing vehicles

Alexandre T.R. Guibert [a], Ashley Cronk [b], Murtaza Bookwala [a], Mohit R. Mehta [c], Y. Shirley Meng [d,e], John W. Lawson [f], H. Alicia Kim [a,b,*]

[a] Structural Engineering Department, University of California San Diego, San Diego, 92093, CA, USA
[b] Materials Science and Engineering Department, University of California San Diego, San Diego, 92093, CA, USA
[c] Intelligent Systems Division, KBR Inc., NASA Ames Research Center, Moffett Field, 94035, CA, USA
[d] NanoEngineering Department, University of California San Diego, San Diego, 92093, CA, USA
[e] Pritzker School of Molecular Engineering, The University of Chicago, Chicago, 60637, IL, USA
[f] NASA Ames Research Center, Moffett Field, 94035, CA, USA

ARTICLE INFO

Keywords:
eVTOL
Lithium-ion battery
Thermal optimization
Electrochemical modeling
Transient optimization
Level-set topology optimization

ABSTRACT

Developing electric vertical take-off and landing vehicles (eVTOL) that can meet the demanding power and energy requirements entails significant challenges, one of which is due to the weight of the battery packs. To address this challenge, optimization techniques can be employed to achieve lightweight designs while satisfying thermal criteria. This study focuses on optimizing a battery heat exchanger housing a high-energy-densitycylindrical cell using the level-set topology optimization method. To accurately account for heat generation from battery electrochemistry, we investigate both a high-fidelity, the Doyle Fuller Newman (DFN) model, and a low-fidelity electrochemical model, the Single Particle Model (SPM), which are compared to experimental results for an eVTOL flight profile. The novelty of the proposed approach resides in the integration of the electrochemical models within a three-dimensional unsteady thermo-electrochemical topology optimization framework. The battery heat exchanger is optimized considering the heat generated by the batteries at the material scale due to the system power requirements. The heat generated by the battery is incorporated as a source term in an unsteady heat conduction finite element model, forming the basis of the optimization process. Our objective is to minimize the integrated thermal compliance over time while satisfying a volume constraint, employing the level-set method. The SPM proves competent in predicting the voltage profile but underestimates the temperature increase. On the other hand, the DFN model accurately predicts both the temperature increase and the voltage profile, making it suitable for the thermal analysis of cells in eVTOL vehicles. Surprisingly, steady-state optimization turns out to be sufficient to generate optimized topologies that perform similarly to transient cases for the case investigated but at a reduced cost. By integrating electrochemical modeling, level-set topology optimization, and heat transfer analysis, our study contributes to the development of lightweight and thermally efficient battery heat exchangers for eVTOL vehicles, which can be extended to battery packs. Importantly, the presented methodology is versatile and can be applied to different battery chemistries, form factors, and power profiles.

1. Introduction

The aerospace sector is undergoing a significant transformation due to the electrification of aircraft and the emergence of urban air mobility (UAM) concepts [1,2]. Among the solutions for UAM, Electric Vertical Take-Off and Landing (eVTOL) vehicles have garnered attention. These vehicles offer a potential solution for alleviating ground traffic congestion and providing a safe, environmentally friendly alternative to conventional individual transportation [3]. As a result, eVTOL vehicles hold the promise of revolutionizing transportation systems in urban areas.

Despite the promising prospects of UAM, its development is accompanied by a range of challenges. Key concerns that the technology currently faces include ensuring safety standards, reducing noise emissions in urban and suburban areas, and enhancing the power and

* Correspondence to: Franklin Antonio Hall 3180 Voigt Dr, La Jolla, CA 92093, USA.
E-mail addresses: aguibert@ucsd.edu (A.T.R. Guibert), acronk@ucsd.edu (A. Cronk), mbookwala@ucsd.edu (M. Bookwala), mohit.r.mehta@nasa.gov (M.R. Mehta), shirleymeng@uchicago.edu (Y.S. Meng), john.w.lawson@nasa.gov (J.W. Lawson), alicia@ucsd.edu (H.A. Kim).

https://doi.org/10.1016/j.applthermaleng.2024.123461
Received 14 February 2024; Received in revised form 15 May 2024; Accepted 19 May 2024
Available online 22 May 2024

Nomenclature

Electrochemical models

Ω_n	Negative electrode domain
Ω_{sep}	Separator domain
Ω_p	Positive electrode domain
ϕ_e	Electric potential in the electrolyte
ϕ_s	Electric potential in the solid phase
N	Molar flux
i	Current density
c	Lithium-ion concentration
SOC	State of charge
a	Electrode surface area per electrode volume
J_k	Interfacial current density
η	Overpotential
U_{oc}	Open circuit potential

Thermal model

κ	Thermal conductivity
T	Temperature
Q	Total volumetric heat generation rate
Q_{Ohm}	Volumetric heat generation rate due to Ohmic heating
$Q_{Reaction}$	Volumetric heat generation rate due to electrochemical reactions
$Q_{Entropic}$	Volumetric heat generation rate due to entropy changes
ρ	Mass density
c_p	Specific heat
t	Time
Γ_T	Surface with prescribed temperature
Γ_N	Surface with prescribed heat flux
Γ_A	Surface with adiabatic boundary condition
q_N	Normal heat flux
$\mathcal{V}$	Space of test functions for the transient heat conduction problem
$\mathcal{S}$	Set of trial functions for the transient heat conduction problem
$\mathcal{H}^1$	Sobolev space of function with one square-integrable derivative
$\mathbf{Q}$	Vector of thermal loads
$\mathbf{T}$	Vector of nodal temperatures

Level-set topology optimization

ϕ	Level-set function
γ	Element volume fraction
Ω	Solid domain
Γ	Solid domain boundary
τ	Pseudo-time
V_n	Normal design velocity
C	Thermal compliance
J	Objective function
χ	Target volume fraction
V_0	Volume of the design domain

Power profile

P_{cr}	Power required during cruise
P_{cl}	Power required during climb
$GTOM$	Gross takeoff mass
L/D	Lift over drag ratio
ROC	Rate of climb
g	Gravity acceleration
η_{eff}	Electric motor efficiency

energy density at the battery pack level [4,5]. Addressing the battery challenge can be approached from two angles: enhancing battery technology at the cell level, such as through advancements in all-solid-state batteries [6], or exploring improvements in the battery containment module, the latter of which is the focus of the present study. One approach to improve the battery containment model is to use parametric optimization. Liu et al. [7] used computational fluid dynamics to perform parametric optimization on a battery pack to minimize the temperature of the cells. Zhu et al. [8] used a heat transfer model considering heat conduction, natural convection, and thermal radiation to model the thermal response of a battery pack and find the optimal inlet flow and temperature. Chen et al. [9] investigated the spacing between the cells in an air-cooled battery pack. They used a simplified battery model and a conjugate heat transfer model and demonstrated a reduction of 42% of the maximum temperature difference between the cells. Li et al. [10] used a conjugate heat transfer model and design of experiments with a multi-objective optimization approach to minimize the volume, maximum temperature difference, and temperature standard deviation among the cells. They studied the tradeoff between the different objectives and considered the spacing between the cells and the mass flow rate of cooling air as design variables. An et al. [11] proposed a simplified model to replace fluid flow and heat transfer models to reduce the computational burden of modeling a battery pack in order to perform parametric optimization. They presented parametric studies on the impact of the aspect ratio of cooling channels, coolant flow rate, and thermal contact resistance. Lu et al. [12] studied a three-dimensional battery pack with a staggered arrangement using a computational fluid dynamics model. Their investigation focused on finding the optimal inlet and outlet locations and the dimensions of cooling channels. Shui et al. [13] performed optimization with a genetic algorithm on a battery pack enclosure to minimize mass, maximum deformation, and maximize the minimum natural frequency. Parametric optimization has the advantage of enabling targeted, efficient exploration of design space for optimal solutions, but the limited design variables limit the range of solutions and the potential performance improvements.

A popular design method to optimize parts and reduce their mass while fulfilling a set of requirements is topology optimization (TO). Since its introduction at the end of the eighties [14], TO has become increasingly popular due to the substantially large design freedom it offers and has been applied in numerous applications [15–17]. In particular, TO has been used to improve the performance of heat transfer systems [18,19]. In the context of battery heat exchanger design, TO of the components of battery packs such as the cooling plate has been investigated. Chen et al. [20] discussed the optimization of two-dimensional cold plates based on a steady-state fluid flow model coupled to a thermal model. Mo et al. [21] topologically optimized two-dimensional cooling plates using a steady-state conjugate heat transfer model and also considered the weighted sum of mean temperature and power dissipation as an objective function to be minimized. They additively manufactured the optimized design and compared it to a reference design which demonstrated significant improvement in terms of heat transfer performances with the topologically optimized cooling plate compared to the reference one, with the maximum temperature decrease of 2.3 K and pressure drop reduction of 47.9%. Wang et al. [22] used a steady-state conjugate heat transfer model in COMSOL Multiphysics to investigate several objective functions for topology

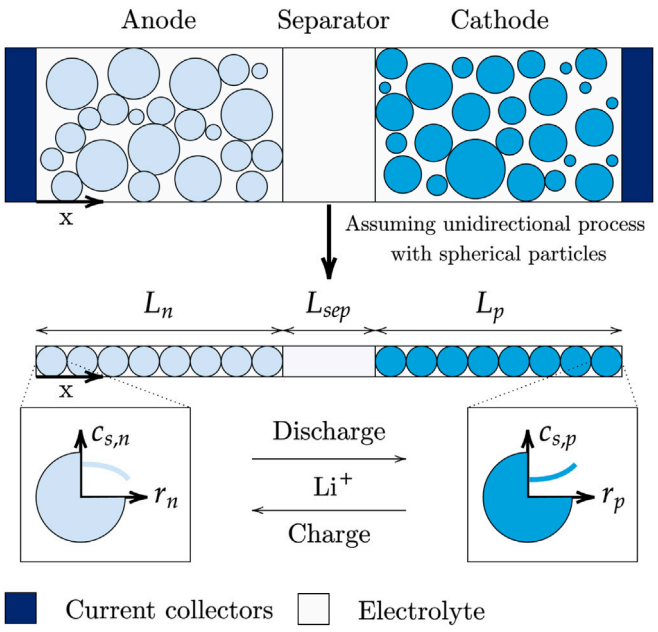

Fig. 1. Schematic of the battery model.

optimization of two-dimensional cold plates for battery packs and recommended using the outlet fluid enthalpy as an objective function in the context of conjugate heat transfer optimization for battery cold plates. Guo et al. [23] topologically optimized two-dimensional cold plates using a steady-state coupled electrochemical-fluid-thermal model to minimize the weighted sum of power dissipation and mean temperature. Zhong et al. [24] investigated the optimization of two-dimensional cooling plates for the thermal design of battery packs using a steady-state conjugate heat transfer model. The model was implemented in COMSOL Multiphysics and the objective function to be minimized was set as the weighted sum of mean temperature and power dissipation. Battery pack components other than cooling plates were also investigated. Mao and Yan [25] performed steady-state thermo-mechanical TO of a battery pack for an electric underwater vehicle to minimize the stress and temperature in the pack. Wanittansirichok et al. [26] optimized a two-dimensional battery thermal management system using a steady-state conjugate heat transfer model. The objective function was set as the weighted sum of thermal compliance and power dissipation and they investigated the influence of different heat loads on the optimized designs. Huang et al. [27] performed thermo-mechanical TO of a battery pack to minimize structural compliance and heat dissipation for steady-state loading. TO has been recently used by Kambampati et al. [28] to design entire battery packs with temperature and stress constraints. The presented methodology relied on the level-set method and they investigated steady-state two-dimensional examples. The heat generation from the cells was assumed to be fixed and was not related to the behavior of the cells. The authors then extended their work to use level-set topology optimization to optimize load-carrying battery packs while considering fluid flow, structural, and thermal requirements [29]. The thermal load was again considered to be given constant and the analysis was conducted at a steady state.

The studies described above have paved the way for topology optimization of heat exchangers for batteries. However, the proposed methodologies in the existing literature limited their optimization to either steady-state heat transfer models, two-dimensional designs, or simplified battery models. In this work, we extend the previous studies by introducing a novel three-dimensional transient topology optimization of a battery heat exchanger based on high-fidelity, physics-derived electrochemical models coupled to a heat transfer model. By doing so our aim is to investigate the dynamic effects associated with future eVTOL flights in optimization. In particular, we investigate the effect of using a steady-state or unsteady heat transfer model for topology optimization purposes. We also investigate the physics-based battery models in the context of eVTOL flights and perform an experimental validation of the models. The utilization of electrochemical models provides valuable information regarding cell response, enabling battery chemistry selection, state of health prediction, and battery optimization. Two models, the Doyle Fuller Newman (DFN) model and the Single Particle Model (SPM), are investigated and compared to experiments for constant discharge cases, and for a power profile for an eVTOL vehicle. The physics-based battery models can be used *a priori*, resulting in savings in cost and time for the development of thermo-electrochemical models and representing a step toward creating digital twins for battery packs.

The remainder of the paper is structured as follows: In Section 2, we introduce the electrochemical models and compare them to experimental results with constant discharge cases. Section 3 describes the transient thermal model. Next, in Section 4, we present the level-set method and the optimization formulation. Finally, we demonstrate the effectiveness of our proposed methodology through numerical examples in Section 5 where we compare the optimized topologies obtained with the two electrochemical models and with steady-state cases. We conclude our findings in Section 6.

2. Electrochemical models

2.1. Doyle-Fuller-Newman model

The Doyle-Fuller-Newman (DFN) model is a continuum model for porous electrodes applied to batteries and was developed in the seminal work by Newman and collaborators [30–32]. Specifically in this work, we are interested in lithium-ion cells. The DFN model is a physics-based model describing the electrochemistry behavior of a cell based on the molar conservation of lithium and electronic and electrostatic charge conservation in the system. The model is solved for the lithium-ion concentrations, electric potentials, current densities, and molar fluxes. It is assumed that the particles are spherical and that the ions transport is mainly unidirectional such that only the effects from one current collector to another are considered where the current collectors are not included in the model. Hence, the model is effectively a one-dimensional model with coordinate x with a pseudo-second dimension for the solid phase diffusion in the active material with coordinate r along the radius of a particle. For this reason, The model is sometimes referred to as a Pseudo-2-Dimensional (P2D) model. The conservation equations in the x-coordinate and r-coordinate are coupled with the description of the intercalation phenomena at the electrode/electrolyte interface with the Butler-Volmer equation. A representation of the model is presented in Fig. 1.

The governing equations of the DFN model are the following:

1. Solid state lithium-ion diffusion in the active material with Fickian diffusion
2. Concentrated electrolyte theory for mass transport in the electrolyte
3. Conservation of charge in the active material based on Ohm's law
4. Conservation of charge in the electrolyte based on MacInnes' equation which is a modified Ohm's law to account for the gradient of concentration in the electrolyte
5. Coupling of the mass and molar conservation at the macroscale and in the pseudo-second dimension with the Butler-Volmer equation which describes the intercalation on the surface of the active particles

More details are given in Appendix A. Throughout the paper, the subscript k is used to indicate the subdomain considered where n, sep, and p correspond to the anode, separator, and cathode domains respectively. The three domains are defined as

$$\Omega_n = \{x \mid x \in [0, L_n)\} \tag{1}$$

$$\Omega_{sep} = \{x \mid x \in [L_n, L_n + L_{sep})\} \tag{2}$$

$$\Omega_p = \{x \mid x \in [L_n + L_{sep}, L]\} \tag{3}$$

where L_n, L_{sep}, and L_p are the thicknesses of the anode, separator, and cathode respectively, and L is the overall thickness. In addition, there is a domain Ω_r corresponding to a spherical particle of active material at each location along x such that

$$\Omega_{r,k} = \{r_k \mid r_k \in [0, R_k]\}, k \in \{n, p\} \tag{4}$$

where R_k is the radius of the particle in an electrode. As mentioned before, the model is solved for the electric potentials ϕ, the molar fluxes N, the current densities i, and the lithium-ion concentrations c. The variables in each region are

$$\phi_{e,k}, c_{e,k}, i_{e,k}, N_{e,k}, \qquad x \in \Omega_k, \quad k \in \{n, sep, p\} \tag{5}$$

$$\phi_{s,k}, i_{s,k} \qquad x \in \Omega_k, \quad k \in \{n, p\} \tag{6}$$

$$c_{s,k}, N_{s,k} \qquad r_k \in \Omega_{r,k}, \quad k \in \{n, p\} \tag{7}$$

The subscript e and s denote the electrolyte and solid phase respectively. Table A.1 summarizes the dimensionless form of the DFN and is given as part of the Appendix A. The model is also described in great details in [33–37].

2.2. Single-particle model

The DFN model is computationally intensive, solving nonlinear partial differential equations. To alleviate the computational burden the Single Particle Model (SPM) offers a simplified alternative [33,34]. The SPM reduces complexity by disregarding electrolyte properties and simplifying transport phenomena. In the SPM, rather than modeling each individual point within the electrode, the focus shifts to a single representative particle. This assumption implies that all particles behave the same way. To derive the SPM from the DFN model, several assumptions are made:

- Charge transfer occurs uniformly across the surface of each active material particle, where intercalation takes place.
- The solid phase within the electrode is assumed to possess high electrical conductivity, resulting in a uniform local volumetric current density through the electrode's thickness.
- Solid phase diffusion dynamics are governed by concentration gradients induced by pore-wall flux density at the particle surfaces. This flux is driven by a constant averaged electrochemical reaction rate.
- The SPM considers instantaneous charge transport between electrodes through the electrolyte. This assumption is based on the fact that electrolytic diffusion occurs significantly faster than solid diffusion.

The last point of the SPM assumptions implies that mass transport in the electrolyte is neglected, resulting in a zero gradient of concentration in the electrolyte. This means that the dynamics of the electrolyte are assumed to have little influence on the behavior of the cell. As a consequence, the Ohmic heating, denoted as Q_{Ohm}, from the electrolyte is neglected in the SPM. Note that the heat generated by the current collectors due to Ohmic heating is also neglected. Instead, only heat generation from the electrochemical reactions, $Q_{Reaction}$, and due to entropic changes, $Q_{Entropic}$, are considered. While this simplification reduces the computational cost, it can result in inaccurate predictions for high discharge rates [36]. However, the SPM can provide valuable insight into the overall behavior of the cell and trends in variables of interest. Therefore, it can serve as a low-fidelity model for optimization at the module level. The dimensionless form of the SPM is given in Appendix B. For more information regarding the SPM and its derivation, we refer to [33,34]. Both the SPM and DFN models are solved using the finite volume method [38] which is appropriate for the conservation laws. The electrochemical models are implemented using the open-source Python library dedicated to battery modeling PyBaMM [39].

2.3. Experimental validation of the electrochemical models

To meet the power, capacity, and therefore energy requirements for our considered eVOTL aircraft, we choose state-of-the-art commercially available lithium-ion cylindrical cells (LG Chem, INR21700M50LT) that possess a high nominal capacity of 5000 mAh and are capable of high current discharge 14.4 A. To be conservative, the minimum capacity of 4850 mAh is used throughout this work to compute the C-rates. This limits the maximum C-rate to 2.97 C. We consider this cell to be theoretically best suited for eVTOL applications due to its cell chemistry, where the NMC811 cathode possesses the highest specific capacity of the stable layered oxides (>200 mAh/g). This chemistry has been extensively studied and used in electric vehicles and proposed for eVOTL applications [4]. In addition, the 21700 cylindrical form factor enables a high energy density for commercially available lithium-ion cells of 260 Wh/kg. The 21700 form factor provides a good compromise between specific capacity and safety since the heat generated is not significantly different compared to 18650 [40,41]. This cell configuration was chosen as an ideal candidate for our aircraft.

To validate the electrochemical models, preliminary simulations and experiments were conducted to capture discharge behavior under constant current discharge conditions and a more complex discharge profile is investigated in Section 5.2. Lithium-ion cylindrical cells were cycled using high-current channels (Arbin Instruments) and under ambient conditions in a thermal chamber. To accurately capture the real-time thermal response, the cell surface temperature was measured using a custom K-type thermocouple connected to a microcontroller with a data acquisition rate of 1 s. The thermocouple leads were connected to the cell surface and adhered using Kapton tape. The cells were charged under 0.1 C (0.485 A) until 4.2 V, then held at 4.2 V until a leakage current of 50 mA was reached. This was done to ensure cells reached 100% SOC (state of charge). The cells were then subsequently discharged at either slow, medium, or fast rates. The slow discharge rate of 0.1 C was used to capture the initial voltage drop without having to consider kinetic limitations. The medium discharge rate of 0.5 C (2.425 A) and the high discharge rate of 1 C (4.85 A) were tested to better emulate discharge rates experienced during flight, which will be further discussed in Section 5.2. The parameters for this cell's electrochemistry were adapted from [42]. The parameters were adjusted to consider calendar aging by modifying the solid electrolyte interface (SEI) thickness and resistivity. The set of parameters for the electrochemical models is given in Appendix C. The results for the rates with low and high-fidelity electrochemical models are presented in Fig. 2.

3. Thermal model

The governing equation for the thermal model is

$$\nabla \cdot (\kappa \nabla T) + Q = \rho c_p \frac{\partial T}{\partial t} \tag{8}$$

where κ is the thermal conductivity, T is the temperature, Q is the volumetric heat generation rate, ρ is the material density, c_p is the specific heat, and t is the time. The heat source term accounts for the Ohmic heating Q_{Ohm} due to resistance in the solid and in the electrolyte, irreversible heating $Q_{Reaction}$ due to the electrochemical reactions, and

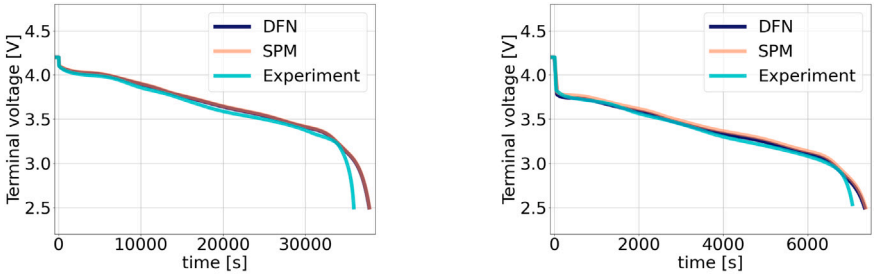

(a) Discharge rate of 0.1C (b) Discharge rate of 0.5C

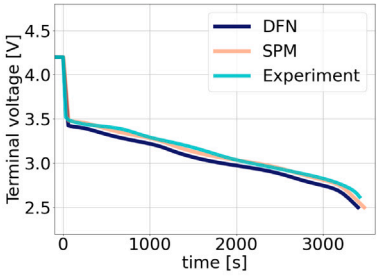

(c) Discharge rate of 1C

Fig. 2. Voltage profiles as a function of time for different constant discharge rates.

reversible heating $Q_{Entropic}$ due to the entropic changes [35]. The terms Q_{Ohm}, $Q_{Reaction}$, and $Q_{Entropic}$ are defined as

$$\begin{aligned} Q_{Ohm} &= \begin{cases} -\left(i_{s,k}\frac{\partial \phi_{s,k}}{\partial x} + i_{e,k}\frac{\partial \phi_{e,k}}{\partial x}\right) & k = n,p \\ -i_{e,sep}\frac{\partial \phi_{e,sep}}{\partial x} & k = sep \end{cases} && k \in \{n, sep, p\} \\ Q_{Reaction} &= a_k J_k \eta_k && k \in \{n,p\} \\ Q_{Entropic} &= a_k J_k T \left.\frac{\partial U_{oc,k}}{\partial T}\right|_{T=T_{ref}} && k \in \{n,p\} \end{aligned} \tag{9}$$

where a_k is the electrode surface area per unit volume, J_k is the interfacial current density, η_k is the overpotential, $U_{oc,k}$ is the open circuit potential, and T_{ref} is the reference temperature. The total heat generation Q is defined as the sum of the different heat generation, i.e., $Q = Q_{Ohm} + Q_{Reaction} + Q_{Entropic}$. The following boundary conditions are considered for the thermal problem.

$$\begin{aligned} T &= T_b \text{ on } \Gamma_T \\ -(\kappa \nabla T)\cdot n &= q_N \text{ on } \Gamma_N \\ (\kappa \nabla T)\cdot n &= 0 \text{ on } \Gamma_A \end{aligned} \tag{10}$$

T_b is a prescribed temperature, q_N is a prescribed heat flux, and Γ_T, Γ_N, and Γ_A correspond to the surfaces associated with prescribed temperature boundary condition, prescribed flux boundary condition, and adiabatic boundary conditions respectively. The thermal model is solved using the finite element method [43]. Let $\mathcal{V}$ and $\mathcal{S}$ be the space of test functions and the set of trial functions, respectively such that

$$\begin{aligned} \mathcal{V} &= \{v(x) \mid x \in \Omega, v \in \mathcal{H}^1(\Omega), v = 0 \text{ on } \Gamma_T\} \\ \mathcal{S} &= \{u(x,t) \mid x \in \Omega, t > 0, u \in \mathcal{H}^1(\Omega), u = T_b \text{ on } \Gamma_T\} \end{aligned} \tag{11}$$

The weak form of the unsteady thermal model with heat generation due to the electrochemical behavior of a lithium-ion battery is,

Given $Q, \kappa, q_n, \rho, c_p$ find $u \in \mathcal{S}$ such that $\forall v \in \mathcal{V}$

$$\int_\Omega Q v \, d\Omega - \int_\Omega \kappa \nabla v \cdot \nabla u \, d\Omega - \int_{\Gamma_N} v q_N \, d\Gamma_N = \int_\Omega \rho c_p \dot{u} v \, d\Omega \tag{12}$$

We apply the finite difference method with an implicit backward Euler scheme for the time discretization which is unconditionally stable such that

$$\dot{u}_n = \frac{u_n - u_{n-1}}{\Delta t} \tag{13}$$

where n is the time index and Δt is the time step. So, finally, we have the following

$$\int_\Omega Q_n v \, d\Omega - \int_\Omega \kappa \nabla v \cdot \nabla u_n \, d\Omega - \int_{\Gamma_N} v q_N \, d\Gamma_N = \int_\Omega \rho c_p \frac{u_n - u_{n-1}}{\Delta t} v \, d\Omega \tag{14}$$

The weak form is approximated using the standard Galerkin approximation with linear shape functions. The thermal model is implemented using FEniCS [44,45] which is an open-source finite element package for solving partial differential equations. It has been chosen because of its ease of implementation of the weak form and for its efficiency. In addition, FEniCS has a Python interface which allows for easy communication with PyBaMM.

To summarize, a given power profile is passed to the electrochemical model as an input to compute the heat generation from the cells. The volumetric heat generation is then fed into the transient thermal model which is solved for the temperature distribution. A sensitivity analysis is then carried out to solve the design optimization problem and update the battery pack until convergence. More details regarding the optimization method are given in Section 4. The optimization workflow is presented in Fig. 3.

4. Level-set topology optimization

4.1. Level-set method

The level-set method (LSM) was originally developed in the context of front propagation [46]. It then became a popular method for topology optimization for its ability to clearly define the interfaces between the different regions of the design domain [17,47,48]. Indeed, the topology is unambiguously defined throughout the optimization history and no additional filtering is necessary in order to obtain a physical optimized part. An implicit function $\phi(x)$ is used to describe the design

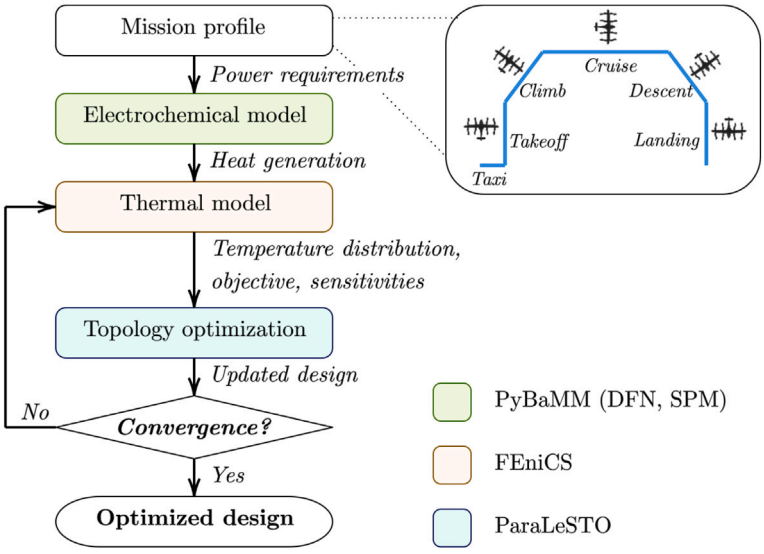

Fig. 3. Optimization workflow.

in the domain. This function is usually initialized as a signed-distance function and is such that

$$\begin{cases} \phi(x) \geq 0, x \in \Omega \\ \phi(x) = 0, x \in \Gamma \\ \phi(x) < 0, x \notin \Omega \end{cases} \tag{15}$$

where Ω is the solid domain and Γ is the boundary. The following Hamilton–Jacobi equation (Eq. (16)), so-called the level-set equation, is used to update the boundary at each iteration [49,50].

$$\frac{\partial \phi(x)}{\partial \tau} + |\nabla \phi(x)| V_n(x) = 0 \tag{16}$$

where τ is the fictitious time and V_n is the normal design velocity. In its discretized form used for the numerical implementation with an explicit forward Euler scheme, it reads,

$$\phi_i^{k+1} = \phi_i^k - \Delta\tau |\nabla \phi_i^k| V_{n,i} \tag{17}$$

where k is the current iteration number, i is a point in the domain, and $\Delta\tau$ is the fictitious time-step. The design velocities are determined by solving a sub-optimization problem. The solution to that problem is a combination of the shape sensitivities and the problem is solved for the boundary movement at each boundary point [49]. The spatial gradient of the level-set function, i.e., $|\nabla \phi_i^k|$, is computed with the Hamilton–Jacobi weighted essentially non-oscillatory (HJ-WENO) scheme [51]. An Eulerian grid, i.e., a fixed grid, is used to mesh the domain. Thus, as the boundary is updated, the zero level-set partially cuts finite elements and the element's effective properties must be computed. The effective thermal conductivity of each element is defined as follows,

$$\kappa_e = \left(\gamma_{min}(1 - \gamma_e) + \gamma_e\right) \kappa \tag{18}$$

where κ_e is the effective thermal conductivity, γ_e is element density which corresponds to the fraction of the volume of the element cut by the level set function, κ is the thermal conductivity of the solid phase, and γ_{min} is a small value used for numerical stability, typically 1×10^{-6} to 1×10^{-9}. The quantity ρc_p is interpolated in the same way.

4.2. Optimization problem formulation

One of the main concerns about lithium-ion batteries for electric vehicles is safety [52]. In particular, thermal runaway has been a major concern as it led to various electric-powered systems ranging from phones to electric vehicles catching fire or exploding [53]. It is one of the common failure mechanisms of batteries and mitigating strategies is an active research topic [54–56]. Thermal runaway is the phenomenon associated with an uncontrollable self-sustaining heating state. Indeed, once some abuse conditions are met, chemical exothermic reactions start leading to additional exothermic reactions in a positive feedback loop until failure. Several abuse scenarios include mechanical impact or overheating, e.g., due to overcharging/overdischarging the cell or a failure in external cooling. The external cooling is the primary concern in this work. The objective for the optimization problem is to minimize the integral of thermal compliance due to the heat source over the analysis time. This objective corresponds to thermal energy due to heat generation from the cells stored in the module over time. Thermal compliance, C, is defined for a steady-state problem as

$$C = \mathbf{Q}^T \mathbf{T} \tag{19}$$

where $\mathbf{Q}$ and $\mathbf{T}$ are the vectors of thermal loads and nodal temperature respectively. This objective is commonly used in thermal optimization problems, e.g., [57,58]. To evaluate the objective over time, thermal compliance is computed at each time step and the values are summed using the trapezoidal rule. Additionally, the mass of the batteries and the associated packs is one of the design constraints to the development of eVTOL vehicles. Indeed, the mass of the battery system is ≈20–25% of the gross weight in the case of an eVTOL while the mass of the fuel represents only ≈2.5–5% in the case of a traditional VTOL vehicle [59]. Moreover, the energy density of a lithium-ion battery is only one-hundredth of the energy density of aviation fuel [60,61]. Thus, it is essential to save as much mass as possible to save energy in order to increase the mission range of eVTOL aircraft. For this reason, a volume constraint is included in the optimization formulation to obtain a lightweight design. In a discrete form and for a transient problem the optimization problem reads

$$\begin{aligned} \underset{\Omega}{\text{minimize}} \quad & \frac{\Delta t}{2}\left(\mathbf{Q}_{t_1}^T \mathbf{T}_{t_1} + 2 \sum_{t_i=2\Delta t}^{t_f-\Delta t} \mathbf{Q}_{t_i}^T \mathbf{T}_{t_i} + \mathbf{Q}_{t_f}^T \mathbf{T}_{t_f}\right) \\ \text{subject to} \quad & V - \chi V_0 \leq 0 \\ & \boldsymbol{R}_i(\boldsymbol{\gamma}, \boldsymbol{T}(\boldsymbol{\gamma})) = \mathbf{0} \end{aligned} \tag{20}$$

where V_0 is the volume of the entire design domain, χ is the prescribed volume fraction, $\boldsymbol{R}_i$ is the residual of Eq. (14) at t_i with the index $i \geq 1$, V is the volume of the optimized topology, t_0 is the initial time, and t_f is the final time. In addition, let

$$\langle \boldsymbol{a} \rangle \triangleq \frac{\Delta t}{2}\left(\mathbf{a}_{t_1} + 2 \sum_{t_i=\Delta t}^{t_f-\Delta t} \mathbf{a}_{t_i} + \mathbf{a}_{t_f}\right) \tag{21}$$

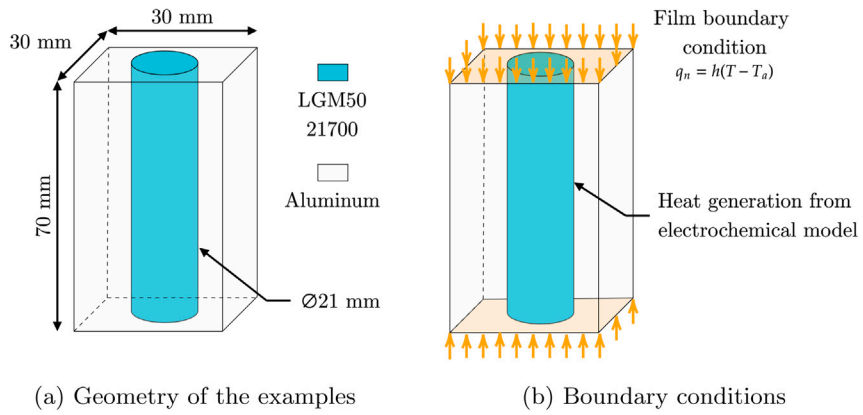

Fig. 4. Geometry of the cell with pack material and boundary conditions for the thermal analysis, wherever the boundary conditions are not specified adiabatic boundary conditions are used.

Table 1
Material thermal properties.

Property	Aluminium	LGM50 21700
Thermal conductivity κ [W m^{-1} K^{-1}]	237.0	1.164[a]/23.1[b]
Volumetric heat capacity ρc_p [J m^{-3} K^{-1}]	2,457,000	1,767,574[c]

[a] Thermal conductivity in the transverse direction [64,65].
[b] Thermal conductivity in the longitudinal direction [64,65].
[c] The effective specific heat is computed as $\rho c_{p,eff} = \left(\sum_k^{n,sep,p} \rho_k c_{p,k} L_k\right)/L$ [36].

Finally, the optimization problem in a concise form is:

$$\begin{aligned} \underset{\Omega}{\text{minimize}} \quad & J = \left\langle \mathbf{Q}^T \mathbf{T} \right\rangle \\ \text{subjectto} \quad & V - \chi V_0 \leq 0 \\ & \boldsymbol{R}_i(\boldsymbol{\gamma}, \boldsymbol{T}(\boldsymbol{\gamma})) = \mathbf{0} \end{aligned} \tag{22}$$

The design variables for the level-set method are the boundary points movement. Thus, the sensitivity of the objective function J with respect to a boundary movement z at a point j must be computed. This quantity is denoted $\frac{dJ}{dz_j}$. First, the sensitivities with respect to the element density γ_e are computed at the centroid of each element using semi-symbolic automatic differentiation via the open-source package dolfin adjoint [62] which yields $\frac{dJ}{d\gamma_e}$. Then, the sensitivities at each discretized boundary point j with respect to a boundary movement are computed via a least squares interpolation scheme [63].

5. Numerical examples

5.1. Material properties and problem setup

Aluminium is chosen for the pack material and the LGM50 cell introduced in Section 2.3 is considered. The electrochemical properties of the cell are adapted from Chen et al. [42]. The complete set of parameters is given in Appendix C. The thermal properties of the cell and aluminium are summarized in Table 1 where the pack material and the cell are considered isotropic and transversely isotropic, respectively.

For the analysis, a cell is studied within the surrounding aluminium. Cooling of the cell occurs at both the top and the bottom. Consequently, film boundary conditions are applied for the thermal analysis on these surfaces, with a heat transfer coefficient of 5 W m^{-2} K^{-1} and an ambient temperature of 298.15 K. The heat generation, derived from the electrochemical model, is assumed to be uniformly distributed throughout the cell. The geometry of the system and the thermal boundary conditions are depicted in Figs. 4(a) and 4(b), respectively. Accounting for symmetry, only one-eighth of the cell is modeled.

Table 2
Details for the power profile computation.

Segment	1[a]	2[b]	3[c]	4[d]	5[e]	6[f]	7[c]	8[b]
Duration [s]	15	30	10	264	1002	10	30	30
Distance [mi]	–	–	–	7.4	35.8	–	–	–
% Max. power[g]	10	100	100	63	60	100	100	100
Power [kW]	46.8	829	829	525	282	829	829	829
Energy [kWh]	0.19	6.91	2.30	38.3	78.6	2.30	6.91	6.91

[a] Taxi with cruise rotor.
[b] 50 ft vertical climb/descent at 100 ft/min.
[c] Transition/Hover.
[d] Climb to 3950 ft with ROC = 900 ft/min, V_{climb} = 101.3 mph, $\eta_{eff,cl}$ = 0.79, and $(L/D)_{climb}$ = 8.5.
[e] Cruise for 35.8 miles with V_{cruise} = 128.6 mph, $\eta_{eff,cr}$ = 0.87, and $(L/D)_{cruise}$ = 9.8.
[f] Descent back to 50 ft above ground level.
[g] Max. cruise power is 468 kW with 1 rotor of 468 kW and max. lift power is 829 kW with 8 rotors of 103.6 kW each.

5.2. Power profile

As a load case for the cell, we evaluate the power profile of a flight path and specifications from [59] considering the '*lift+cruise*' vehicle concept. Given the power requirement, the percentage of power required for each flight segment, and the flight segment duration, we can estimate the energy requirement. Power requirements can be calculated using the following equations [59],

$$\begin{aligned} P_{cr} &= GTOM \frac{g}{\eta_{eff,cr}} \frac{V_{cr}}{(L/D)_{cruise}} \\ P_{cl} &= GTOM \frac{g}{\eta_{eff,cl}} \left(ROC + \frac{V_{climb}}{(L/D)_{climb}} \right) \end{aligned} \tag{23}$$

where P_{cr} and P_{cl} are the power required during the cruise and the climb segment, respectively. Power is a function of aerodynamic parameters like lift-to-drag ratio L/D, velocity V, and gross takeoff mass $GTOM$ which is taken as 4268.3 kg assuming a payload of 6 passengers. Climb power, P_{cl} is a function of the rate of climb ROC, the gravity acceleration g, and electric motors efficiency η_{eff}. The details for calculations are shown in Table 2, where the trip duration, distance, and energy requirement are calculated at the battery pack level.

To size the battery pack and hence the flight profile and C-rates requirements, the maximum depth of discharge of 80% is used to preserve the health of the battery. We obtain that the energy of the battery pack is 179 kWh. Note that we do not account for reserve in this analysis. Using the expected weight fraction of the battery to be 20% of the total aircraft, this results in a battery pack possessing an energy density of

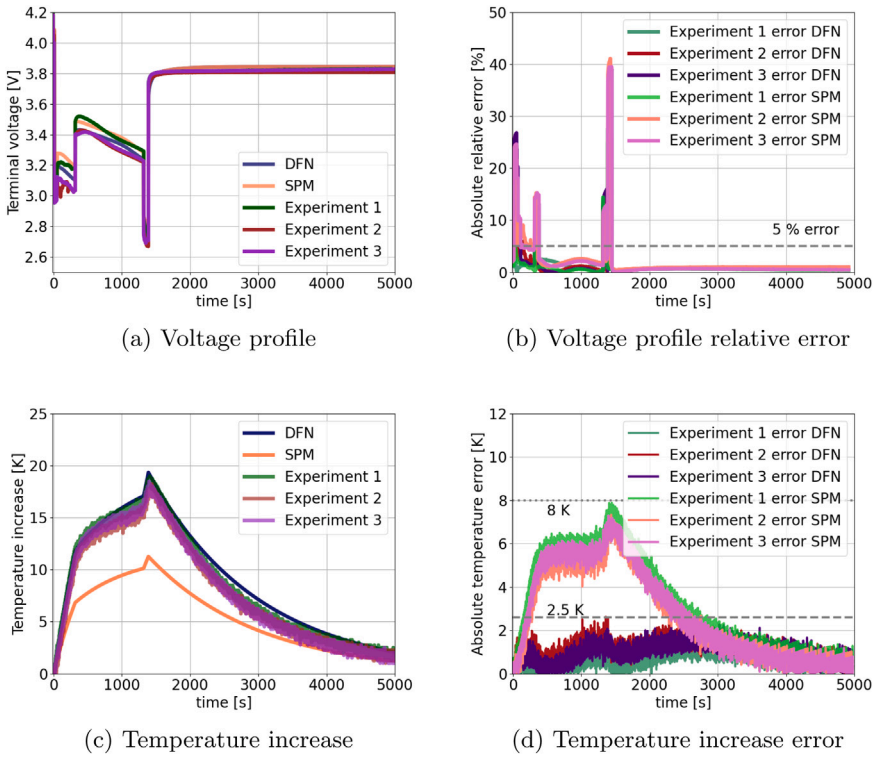

(a) Voltage profile (b) Voltage profile relative error

(c) Temperature increase (d) Temperature increase error

Fig. 5. Cell response to power profile.

Table 3
Power profile used for this work.

Phase	Duration [s]	Calculated C-rate [C]	Adjusted C-rate [C]	Current [A]
Taxi	15	0.2	0.2	0.78
Takeoff	40	4.4	1.7	8.4
Climb	264	3.0	1.5	7.2
Cruise	1002	1.6	0.9	4.5
Landing	70	4.4	1.7	8.4

233 Wh kg^{-1}, with the target cell gravimetric energy density being > 330 Wh kg^{-1} (assuming a cell-to-pack efficiency of 70% [66,67]). The estimated energy density of the battery pack indicates that cell energy density (>330 Wh kg^{-1}) is beyond the current state-of-the-art battery chemistries available commercially [68,69]. The voltage for the mission is chosen to be 800 V from the motor attributes discussed in [59]. The nominal voltage of the 21700 cells allows the determination of the required cells in series to meet the voltage requirements. With a system voltage of 800 V, the battery pack capacity of 223 Ah is obtained, where 45 cells in parallel were assumed for this vehicle. Knowing the power requirement, duration, and the current, C-rate can be calculated since the power is the product of the current and the voltage and the C-rate is the current divided by the battery pack capacity which was estimated to be 223 Ah.

Table 3 summarizes these results for the entire battery pack and the expected power profile where the battery is assumed to be made of identical ideal cells without any losses or defects. This computation led to C-rates greater than 1.7 C which cannot be tested in the experimental facility available for this work due to safety. Thus, the C-rate was kept at a maximum of 1.7 C (1 C = 4.85 A), and the power profile was adjusted such that the cell could complete the power profile as shown in Table 3. The scaled power profile was used for the experiments and the electrochemical models, i.e., DFN and SPM.

It is noted that for the eVTOL flight profiles, the C-rate and power requirements during the takeoff and landing phases are high. These flight segments pose the most significant challenge for the current state-of-the-art battery technology and will be the focus of the primary investigation for optimization in this work. Thus, only the heat generated during the landing segment is considered for transient thermal optimization.

5.3. Cell response to power profile

Given the power profile in Section 5.2, the surface temperature increase and terminal voltage are measured experimentally on a pristine LGM50 21700 cell. The experiment is done three times and a new LGM50 21700 cell is used for each experiment. The voltage profile and the temperature increase from the experiments are compared to the voltage and temperature increase of the electrochemical models in Fig. 5. The voltage and temperature increase after the flight, when the cell is at rest, is also shown.

Although some variability is observed, both the SPM and DFN models effectively represent the experimental voltage profiles reasonably closely. The absolute relative error used for the terminal voltage comparison is defined as the absolute difference between the results from the physics-based models and the experimental data divided by the experimental data. The absolute relative error for the voltage profile is shown in Fig. 5(b).

The large discrepancies between the experiments and modeling results arise from the difference in data acquisition rates. In the electrochemical simulations and thermocouple measurements, time steps are easily implemented. In our computational model, we set all acquisition rates to be 1 s. However, for experimental cell measurements, data acquisition rates are challenging to be exact. This is due to the cycler capabilities, where even though record durations were set to 1 s, factors such as voltage limits and resting periods make it difficult to have the battery run at exactly the prescribed time step. This small mismatch can result in significant errors at the transitions between the different flight segments in the power profile, e.g. from takeoff to climb. Indeed, these large errors are only seen at the flight phase transitions. For example, the highest peak error in Fig. 5(b) corresponds to the transition from the cruise to the landing phase. Therefore, we deduce that the large errors

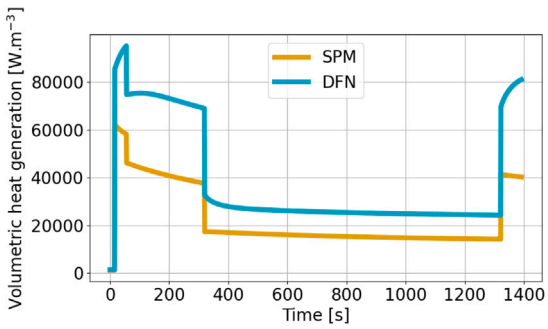

Fig. 6. Volumetric heat generation as a function of time for the power profile considered.

originate from the mismatch in time between those segments. The other peaks with a relative error greater than 5% all correspond to transitions from one flight segment to another. Outside these phase transitions, the relative error for both electrochemical models is consistently less than 5% as shown in Fig. 5(b).

The absolute temperature difference between the experimental and computational data is shown in Fig. 5(d) where it is seen that the DFN model reasonably approximates the surface temperature increase with a maximum error of 2.5 K. The SPM significantly underestimates the temperature rise due to neglecting electrolyte behavior with a maximum error of up to 8 K or an absolute relative error of about 41%. This is expected since it has been shown for pouch cells that an electrolyte correction is needed to account for mass and electrostatic contributions to the total voltage loss and the total heat generated [36]. The SPM does not account for any Ohmic heating from the electrolyte and Ohmic heating from the current collectors, and the reaction-based heating is approximated using an averaged particle size. Consequently, the SPM generates less heat, particularly during high C-rate segments like takeoff and landing, leading to a significant underprediction of the cell surface temperature. Nevertheless, if only the terminal voltage is required, such as for testing different flight profiles and determining if the voltage cut-off is reached, the SPM offers meaningful results, especially in the case of low to moderate C-rates (0–1.5 C). Notably, the computational time of the SPM for the studied power profile is only 1.2 s on a typical laptop, while the DFN model applied to the same power profile requires over 11 min on the same laptop.

5.4. Topology optimization results

5.4.1. Single particle model vs. Doyle-Fuller-Newman model

The electrochemical models with the selected power profile can now be used for optimization. For the first example of optimization, four target volume constraint values are considered: 45% ($\chi = 0.45$), 50% ($\chi = 0.50$), 55% ($\chi = 0.55$), and 60% ($\chi = 0.60$). To avoid storing an excessive amount of thermal energy in the system over time, the objective function to be minimized is thermal compliance integrated over time as described in Section 4.2. The structure is discretized with $30 \times 30 \times 70$ hexahedral linear finite elements. The mesh convergence study is presented in Appendix D. The volumetric heat generated by the battery during the landing phase is calculated using the DFN and the SPM models and the heat generation during the complete flight is shown in Fig. 6. Note that once either of the two electrochemical models is chosen for optimization, it remains unchanged for the duration of the process. For example, in scenarios utilizing the DFN model, the heat generation computed by the DFN model serves as a consistent source term for every iteration of the transient heat transfer model throughout the optimization process.

The eight optimized topologies obtained with the heat generation from each electrochemical model with symmetry and with the four different volume fractions are shown in Fig. 8. The convergence histories for $\chi = 0.45$ using the SPM and DFN models are shown in Fig. 7 where in both cases we observe that the objective function converges relatively smoothly after the volume constraint has been satisfied. The convergence histories for the other volume fractions showed similar trends and thus are not shown for conciseness. For the volume fraction $\chi = 0.45$ shown in Figs. 8(a) and 8(e), there is no apparent difference between the design optimized using the SPM and DFN models. For $\chi = 0.50$, the main difference between the two model results is the size of the groove near the top half of the cell in Figs. 8(b) and 8(f). For the results with higher volume fractions shown in Figs. 8(c), 8(g), 8(d), and 8(h), the major distinction is the shape of the bulges nearer the bottom.

To quantify the impact of these features, i.e., the grooves and the bulges, on the performance of the heat exchanger, the optimized designs are further analyzed. To maintain consistency, the optimized results from both models are analyzed with the finite element method for the same heat loads obtained from the higher fidelity model (DFN in Fig. 6).

In Fig. 9, the temperature distribution within the optimized battery exchanger is presented at the last time step, i.e. the step with maximum temperature distribution. The optimized shape is shown by the outline within the whole design domain. For a given volume fraction, the temperature distribution within the exchanger optimized with SPM loading is similar to its DFN counterparts. In Fig. 10, validation results for shapes obtained from both power profiles are compared together. For a given volume fraction, an average difference of 0.006 K is observed between the maximum temperature in the geometries optimized for SPM and DFN loading. Hence it can be concluded that the optimization results for loading obtained from SPM, a lower-fidelity battery model are comparable to the results obtained from the DFN power profile in terms of thermal performance, even with the apparent design differences.

Note that higher volume fraction constraints enable better heat dissipation effects but at the cost of utilizing more material which will directly affect the gravimetric and volumetric energy density of the battery pack. With a volume fraction of 45%, a 14% reduction of gravimetric energy density is estimated compared to the cell alone, from 260 Wh/kg to 224 Wh/kg. With the higher volume fraction constraint of 55%, the impact is nearly doubled with a 30% reduction, reducing the gravimetric energy density to 185 Wh/kg. These are important considerations when implementing heat exchangers into the battery pack/module design. Coman et al. [66] and Darcy [67] designed and tested battery modules with a gravimetric energy density of around 190 Wh/kg with a cell-to-module mass ratio of ≈0.7. The gravimetric energy densities obtained with the topologically optimized heat exchangers show an 18% improvement for the case with a 45% volume fraction. However, the wiring and battery management system are not modeled and should also be considered for actual pack designs.

5.4.2. Comparison to steady-state optimization

To evaluate the significance of utilizing an unsteady diffusion model for optimization, a steady-state topology optimization scenario is studied. In this case, the time-dependent temperature term is eliminated from the weak form given in Eq. (14), resulting in the following weak form.

$$\int_{\Omega} Q_n v \, d\Omega - \int_{\Omega} \kappa \nabla v \cdot \nabla u_n \, d\Omega - \int_{\Gamma_N} v q_N \, d\Gamma_N = 0 \tag{24}$$

The objective of the steady state optimization is to minimize the thermal compliance, i.e., $J = \mathbf{Q}^T \mathbf{T}$. The volumetric heat generation is taken as the maximum heat generation during flight predicted by the DFN model. The optimized topologies obtained for the steady-state cases for the same target volume fraction as in Section 5.4.1, that is 45% ($\chi = 0.45$), 50% ($\chi = 0.50$), 55% ($\chi = 0.55$), and 60% ($\chi = 0.60$), are shown in Fig. 11. Expanding conduction paths from the middle of

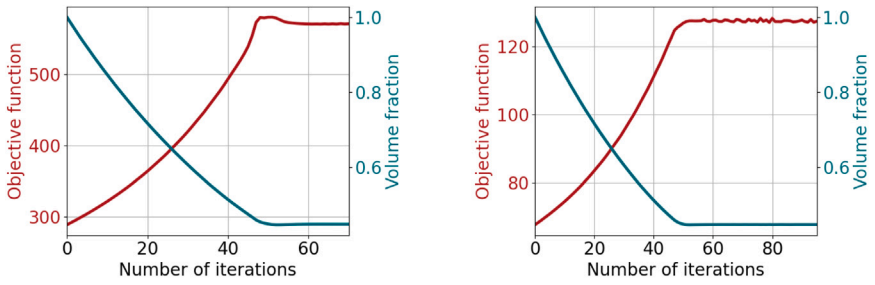

(a) DFN (b) SPM

Fig. 7. Convergence history for $\chi = 0.45$.

(a) DFN ; $\chi = 0.45$ (b) DFN ; $\chi = 0.50$ (c) DFN ; $\chi = 0.55$ (d) DFN ; $\chi = 0.60$

(e) SPM ; $\chi = 0.45$ (f) SPM ; $\chi = 0.50$ (g) SPM ; $\chi = 0.55$ (h) SPM ; $\chi = 0.60$

Fig. 8. Topology optimization results of the battery exchanger for four volume fractions (χ) and two electrochemical models (DFN, SPM).

the cell to the top of the cell are observed. The grooves and bulges seen in Fig. 8 for transient optimizations are not visible in the designs from the steady state optimization.

To assess the computational costs, we present the average computational cost per optimization iteration for each case in Table 4. Remarkably, a transient optimization iteration over the landing phase costs roughly 30 times more than the steady-state optimization.

In addition, the thermal behavior of the optimized structures obtained with the steady-state optimization, Fig. 11, is compared to the results from the previous section, Fig. 8. The optimized designs are analyzed with the finite element method and subjected to the heat loads obtained from the DFN model in Fig. 6. In Fig. 12, the temperature distributions on the film boundary are shown. An average difference of 0.02 K is observed in the maximum temperature between the designs obtained from DFN or steady-state loading.

In Fig. 13, a comparison of the thermal compliance integrated over time, $J = \langle \mathbf{Q}^T \mathbf{T} \rangle = \int_t \mathbf{Q}^T \mathbf{T} dt$ is given. Thermal compliance here is obtained only for the landing segment which was used for the transient

Table 4
Comparison of the computational time for all cases.

Target volume fraction	Optimized for	Average wall time per optimization iteration [s]
$\chi = 0.45$	DFN	371.5
	SPM	375.2
	Steady-state	13.40
$\chi = 0.50$	DFN	364.1
	SPM	374.9
	Steady-state	12.11
$\chi = 0.55$	DFN	368.2
	SPM	360.3
	Steady-state	11.62
$\chi = 0.60$	DFN	369.5
	SPM	367.1
	Steady-state	11.84

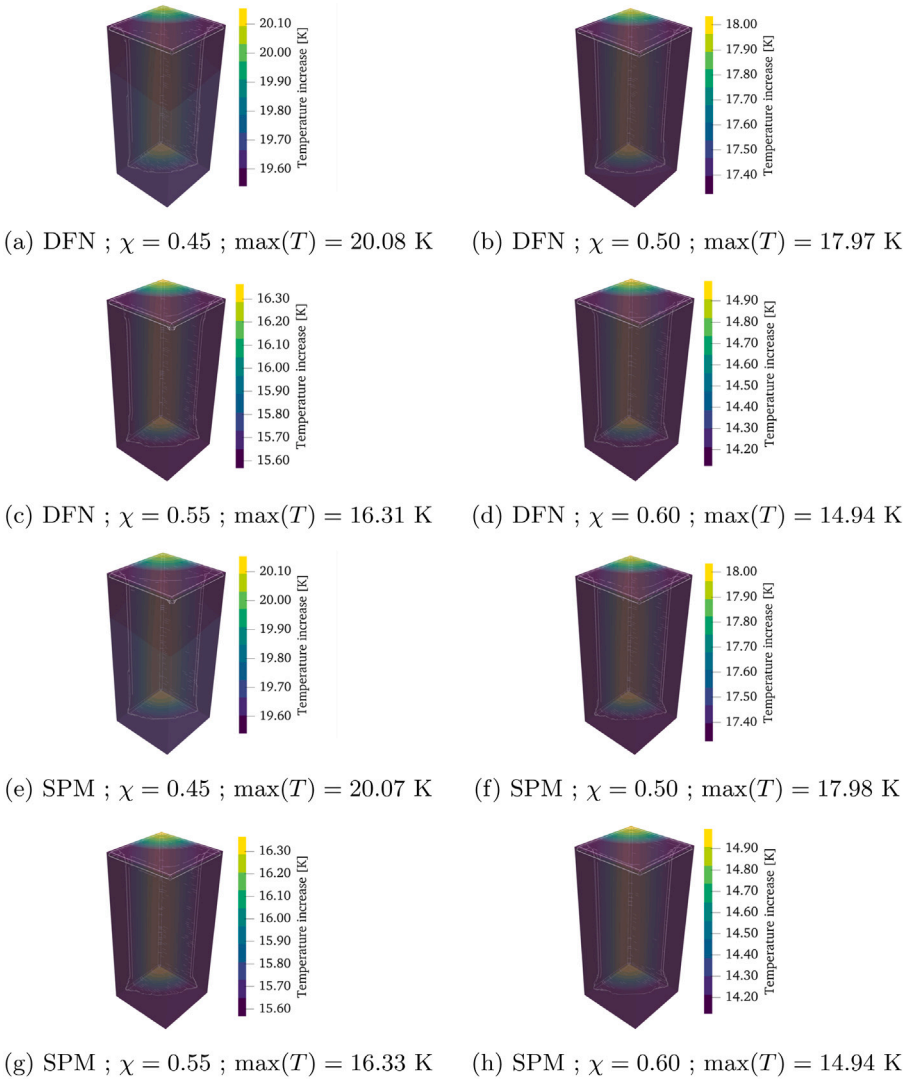

Fig. 9. Temperature distribution of the optimized battery exchanger for four volume fractions (χ) and two electrochemical models (DFN, SPM) at the final time step, $\max(T)$ denotes the maximum nodal temperature.

optimizations. The differences in total compliances of optimized geometries obtained from three different loading conditions are negligible even if the geometrical differences are noticeable. However, for the higher target volume fractions of 55% and 60%, where enough material is available to manifest more features that can optimize the objective, we see lower values of thermal compliance in structures optimized for DFN loading. For a target volume fraction of 60%, the thermal compliance is 0.65 W K s less for the design optimized for DFN as compared to the design optimized for steady-state.

The maximum temperatures at each time step for the 12 optimization cases, i.e., the 4 target volume fractions and steady-state, DFN, and SPM, are shown in Fig. 14. The maximum temperature at each time step for the battery without a heat exchanger is also shown for reference. The steady-state optimization proves to be sufficient for the cases investigated here, as it yields optimized topologies that perform similarly, in terms of maximum temperature and temporally integrated thermal compliance, to the structures obtained through optimization considering the transient loading over landing, at a fraction of the computational cost. The transient effects appear to be secondary as the heat is continuously conducted out of the domain for an extended period, which is the case for the power profile of a flight mission. Hence, for power profiles resembling the one we examined, which are divided into a few segments with constant current, steady-state heat conduction optimization proves to be a viable and more computationally efficient choice. Nevertheless, the heat generation as a function of time as predicted by the electrochemical models allows for a comprehensive post-optimization analysis and evaluation of the optimized topologies throughout the entire flight.

5.4.3. Comparative analysis of the impact of the ambient temperature

The influence of ambient temperature on volumetric heat generation, as predicted by the DFN and SPM models, is now being investigated. Throughout the previous sections, the ambient temperature of 298.15 K is used for the thermal and electrochemical models. The temperature of 298.15 K is selected since it is the temperature at which the experiments were conducted.

For the investigation of the ambient temperature influence, the parameters remain consistent with those used throughout this work and are provided in Appendix C. Only the ambient temperature varies from 293.15 K to 318.15 K with steps of 5 K. The results of this ambient temperature sweep are given in Fig. 15.

The maximum heat generation predicted by the DFN model ranges from 77 kW m^{-3} to 100 kW m^{-3} with a value of 95 kW m^{-3} for an ambient temperature of 298.15 K which is the nominal case used for the analysis. With the SPM, the heat generation ranges from 43 kW m^{-3} to 67 kW m^{-3} with a value of 62 kW m^{-3} for the case used for

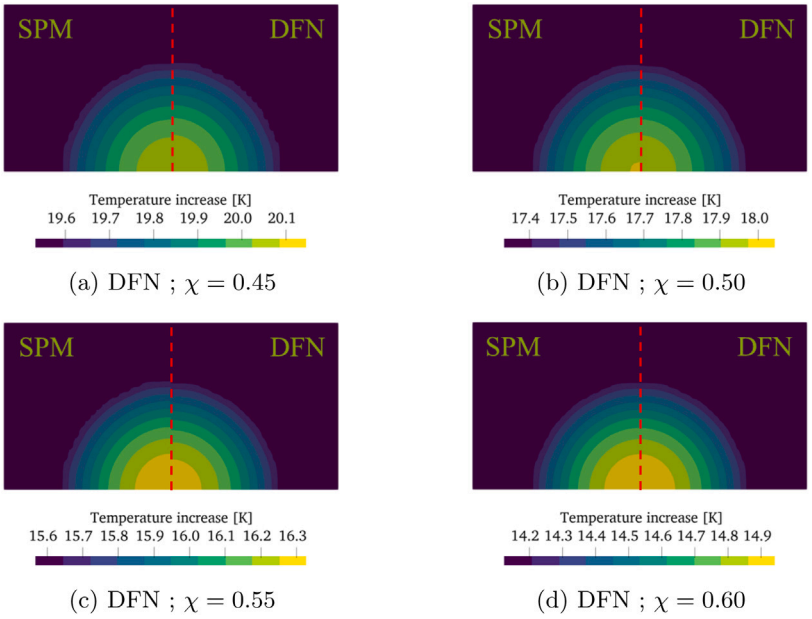

Fig. 10. Temperature distribution at the convection boundary conditions of the battery exchanger optimized for DFN and SPM at the final time step.

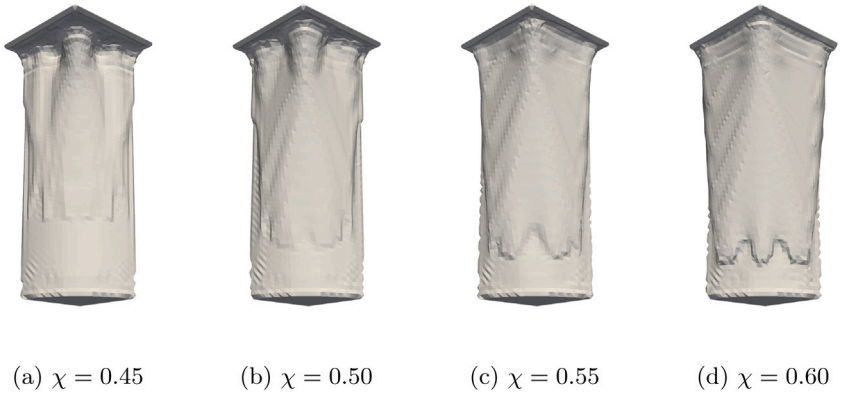

Fig. 11. Steady-state topology optimization results of the battery exchanger for four volume fractions (χ).

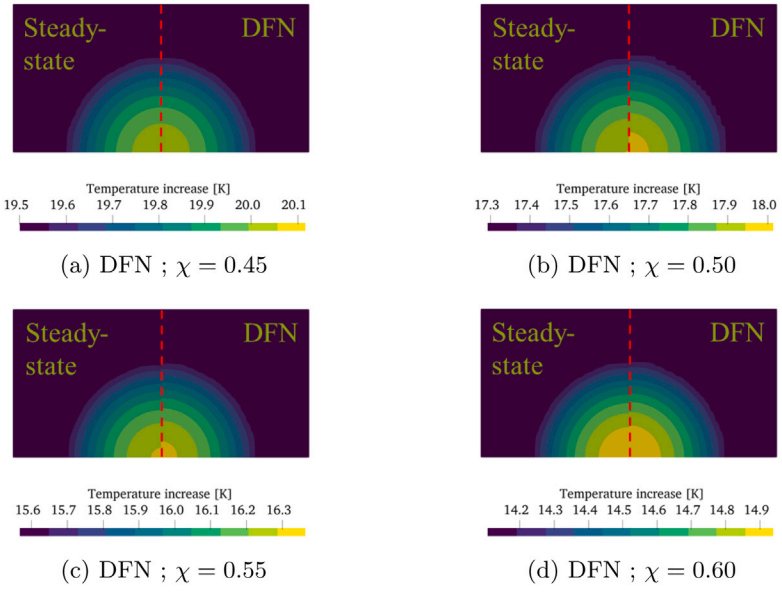

Fig. 12. Temperature distribution at the convection boundary conditions of the battery exchanger optimized for DFN and steady-state at the final time step.

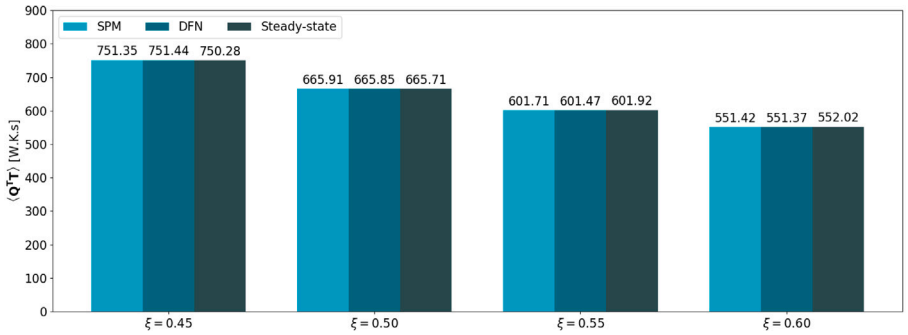

Fig. 13. Compliance integrated over the landing phase for all optimized heat exchangers.

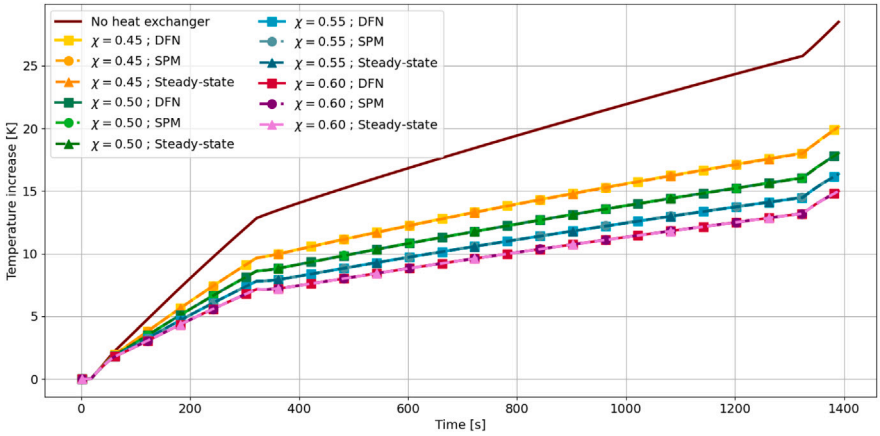

Fig. 14. Maximum temperature as a function of time for all cases considered, the maximum temperature for the battery without heat exchanger is shown for reference.

optimization. At an ambient temperature of 318.15 K, the maximum heat generation predicted by the DFN model differs by up to 19% compared to the optimization case, while the SPM model exhibits even greater sensitivity, with heat generation varying by 31%.

As discussed in Section 5.4.2, the performance of the optimized heat exchanger using a steady-state heat conduction model is comparable to that of heat exchangers employing either the SPM or DFN models for the case investigated. Therefore, significant deviations in the topologically optimized heat exchanger's performance due to changes in ambient temperature are unlikely.

6. Conclusions

We have introduced a novel three-dimensional transient thermo-electrochemical topology optimization formulation for designing a heat exchanger dedicated to lithium-ion batteries in an eVTOL vehicle. We explored and evaluated two electrochemical models, namely the DFN and SPM models, which are based on mass conservation, charge conservation, and electrochemical reactions. These models were utilized to predict the voltage profile and the volumetric heat generation rate for a given flight profile. We compared the results of the two electrochemical models with the experimental data obtained from constant discharge rates and a scaled flight profile for validation. The level-set topology optimization method was then used as a design tool and the temperature distribution in the heat exchanger was computed using a transient heat conduction finite element model. We conducted numerical simulations focusing on a cell and its surrounding material, considering natural convection for cooling. We analyzed the influence of using the SPM or DFN as an electrochemical model for optimization and compared optimized topologies obtained with transient and steady-state heat conduction models to a reference case without a heat exchanger over the entire flight. The conclusions of the investigation are as follows:

1. Both the SPM and DFN models showed a relative error of less than 5% for the voltage profile compared to experimental data excluding the transition between the flight segments, with the SPM model offering an efficient alternative, being up to two orders of magnitude faster than the DFN model for the cases investigated.
2. The DFN model demonstrated accuracy for cell temperature increase prediction with a relative error of less than 10% for the maximum temperature compared to experimental data for the profile studied.
3. The SPM model failed to accurately capture the temperature increase with a relative error of around 41% at the peak temperature although still managed to represent the overall trend.
4. The use of topologically optimized heat exchangers for lithium-ion batteries in eVTOL vehicles appears promising with relative maximum temperature reductions of more than 42% and 47% for volume fractions of 55% and 60%, respectively.
5. The steady-state heat conduction optimization resulted in topologies with thermal performance comparable to the transient examples, i.e., with less than 1% difference in both the maximum temperature and thermal compliance for a given target volume fraction, but at a lower computational cost, on average more than 30 times faster for the cases investigated.

In future work, we plan to explore battery pack configurations and examine the interplay between the individual cells. Additionally, note that in practice, battery degradation should be considered for repeated power profiles and that the material properties would change as a function of aging [70,71]. Therefore, the impact of repeated flights on cell degradation and mitigation strategies is in the future research scope.

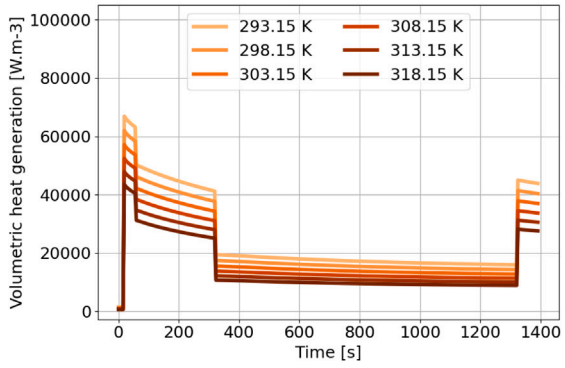

(a) SPM

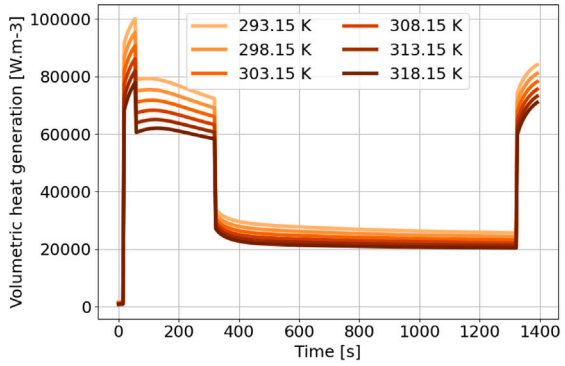

(b) DFN

Fig. 15. Volumetric heat generation for the SPM and DFN models as a function of the ambient temperature.

CRediT authorship contribution statement

Alexandre T.R. Guibert: Writing – original draft, Visualization, Validation, Software, Methodology, Investigation, Formal analysis, Conceptualization. **Ashley Cronk:** Writing – original draft, Methodology, Investigation, Data curation. **Murtaza Bookwala:** Writing – original draft, Visualization, Software, Methodology, Investigation. **Mohit R. Mehta:** Writing – review & editing, Software, Methodology, Data curation. **Y. Shirley Meng:** Writing – review & editing, Supervision, Resources, Funding acquisition. **John W. Lawson:** Writing – review & editing, Supervision. **H. Alicia Kim:** Writing – review & editing, Supervision, Resources, Project administration, Funding acquisition, Conceptualization.

Declaration of competing interest

The authors declare that they have no known competing financial interests or personal relationships that could have appeared to influence the work reported in this paper.

Data availability

Data will be made available on request.

Acknowledgments

We acknowledge the support from NASA award No. 80NSSC21M0070 and LG Energy Solution through the Frontier Research Laboratory (FRL) program. JWL and MRM were supported by funding from the NASA Aeronautics Research Mission Directorate's (ARMD) Transformational Tools and Technologies (TTT) project.

Appendix A. Details on the Doyle Fuller Newman model

Throughout the Appendices, the notations introduced in Section 2 are used. The DFN model is given here for completeness and more details regarding the model are given in [34–37]. For a comprehensive review of the existing physics-based lithium-ion battery models, we refer to [72].

Molar conservation

Fick's law of diffusion describes the transient diffusion process from a higher concentration to a lower concentration in an electrode particle. In spherical coordinates, Fick's first and second laws are given as follows:

$$N_{s,k} = -D_{s,k}\frac{\partial c_{s,k}}{\partial r_k} \qquad k \in \{n,p\} \tag{A.1}$$

$$\frac{\partial c_{s,k}}{\partial t} = -\frac{1}{r_k^2}\frac{\partial}{\partial r_k}\left(r_k^2 N_{s,k}\right) \qquad k \in \{n,p\} \tag{A.2}$$

where $D_{s,k}$ is the diffusivity of lithium ions in a particle. As for the boundary conditions, there is no molar flux at the center due to symmetry, and lithium intercalation takes place at the surface such that:

$$N_{s,k}|_{r_k=0} = 0 \qquad k \in \{n,p\} \tag{A.3}$$

$$N_{s,k}|_{r_k=R_k} = \frac{J_k}{a_k F} \qquad k \in \{n,p\} \tag{A.4}$$

where F is Faraday's constant and J_k is the interfacial current density from the charge transferred to the electrolyte at the macroscale, and a_k is the active surface area per unit volume. In the electrolyte, the molar conservation of lithium can be described as follows:

$$\epsilon_k \frac{\partial c_{e,k}}{\partial t} = \frac{\partial N_{e,k}}{\partial x} + \frac{1}{F}\frac{\partial i_{e,k}}{\partial x} \qquad k \in \{n,sep,p\} \tag{A.5}$$

$$N_{e,k} = \epsilon_k^{bk} D_{e,k}\frac{\partial c_{e,k}}{\partial x} + \frac{t^+}{F} i_{e,k} \qquad k \in \{n,sep,p\} \tag{A.6}$$

where ϵ_k is the volume fraction of electrolyte, $D_{e,k}$ is the diffusivity of lithium-ion in the electrolyte which is a function of $c_{e,k}$ such that $D_{e,k} \equiv D_{e,k}(c_{e,k})$, t^+ is the cation transference number which is the fraction of the current being carried by the cation, i.e, by the positively charged ion, and bk is the Bruggeman coefficient usually taken as 1.5 for porous structures such as a lithium-ion battery. For consistency, continuity of flux and concentration is imposed between the different domains:

$$\begin{aligned} N_{e,n}|_{x=L_n} &= N_{e,sep}|_{x=L_n} & N_{e,sep}|_{x=L_n+L_{sep}} &= N_{e,p}|_{x=L_n+L_{sep}} \\ c_{e,n}|_{x=L_n} &= c_{e,sep}|_{x=L_n} & c_{e,sep}|_{x=L_n+L_{sep}} &= c_{e,p}|_{x=L_n+L_{sep}} \end{aligned} \tag{A.7}$$

Additionally, there is no flux at the current collectors:

$$N_{e,n}|_{x=0} = 0 \qquad N_{e,p}|_{x=L} = 0 \tag{A.8}$$

Charge conservation

The interfacial current density J_k considers the total charge transfer due to intercalation kinetics at a location x and acts as a source term for current densities in the electrolyte and electrode where the active material is present:

$$\frac{\partial i_{e,k}}{\partial x} = -\frac{\partial i_{s,k}}{\partial x} = \begin{cases} J_k, & k = n,p \\ 0, & k = sep \end{cases} \qquad k \in \{n,sep,p\} \tag{A.9}$$

The current densities are computed using Ohm's law for solid material (Eq. (A.10)) and MacInnes' equation (Eq. (A.11)) for the electrolyte which relates the current density to the electric potential and electrolyte concentration in the following fashion

$$i_{s,k} = -\sigma_k \frac{\partial \phi_{s,k}}{\partial x} \qquad k \in \{n,p\} \tag{A.10}$$

$$i_{e,k} = \epsilon_k^{bk}\zeta_e\left[-\frac{\partial \phi_{e,k}}{\partial x} + 2(1-t^+)\frac{R_g T}{F}\frac{\partial \log c_{e,k}}{\partial x}\right] \qquad k \in \{n,sep,p\} \tag{A.11}$$

where ζ_e is a reference electric conductivity of the electrolyte, σ_k is the electric conductivity of the electrode material, R_g is the universal gas constant, and T is the temperature. Again, continuity is imposed between the different domains and there is no current density in the electrode at the anode/separator and separator/cathode boundaries such that

$$\begin{aligned} &i_{e,n}|_{x=L_n} = i_{e,sep}|_{x=L_n} \qquad i_{e,sep}|_{x=L_n+L_{sep}} = i_{e,p}|_{x=L_n+L_{sep}} \\ &\phi_{e,n}|_{x=L_n} = \phi_{e,sep}|_{x=L_n} \qquad \phi_{e,sep}|_{x=L_n+L_{sep}} = \phi_{e,p}|_{x=L_n+L_{sep}} \\ &i_{s,n}|_{x=L_n} = 0 \qquad i_{s,p}|_{x=L_n+L_{sep}} = 0 \end{aligned} \tag{A.12}$$

Additionally, the current i_{app} is applied at the current collectors to the active material where the electrolyte current density is zero which gives four additional boundary conditions

$$\begin{aligned} &i_{s,n}|_{x=0} = i_{app} \qquad i_{s,p}|_{x=L} = i_{app} \\ &i_{e,n}|_{x=0} = 0 \qquad i_{e,p}|_{x=L} = 0 \end{aligned} \tag{A.13}$$

Note that because of continuity and charge conservation, we have the following relationships

$$\begin{aligned} &i_{s,k} + i_{e,k} = i_{app} \qquad k \in \{n,p\} \\ &i_{e,sep} = i_{app} \end{aligned} \tag{A.14}$$

The terminal voltage V is defined as the potential difference between the two current collectors where the reference potential is $\phi_{s,n}|_{x=0} = 0$

$$\begin{aligned} V &= \phi_{s,p}|_{x=L} - \phi_{s,n}|_{x=0} \\ &= \phi_{s,p}|_{x=L} \end{aligned} \tag{A.15}$$

Intercalation kinetics

The Butler-Volmer equation describes the intercalation kinetics of lithium. This reaction couples the macroscale and microscale and is as follows

$$J_k = J_{k,0} \sinh\left(\frac{F}{2R_g T}\eta_k\right) \qquad k \in \{n,p\} \tag{A.16}$$

where $J_{k,0}$ is the exchange current density and η_k is the overpotential which are defined as

$$\begin{aligned} &J_{k,0} = \mu_k (c_{s,k} c_{e,k})^{1/2} (c_{s,k}^{max} - c_{s,k}|_{r_k=R_k})^{1/2} \qquad k \in \{n,p\} \\ &\eta_k = \phi_{s,k} - \phi_{e,k} - U_{oc,k} \qquad k \in \{n,p\} \end{aligned} \tag{A.17}$$

where μ_k is the reaction rate, $c_{s,k}^{max}$ is the maximum lithium-ion concentration in the active material, and $U_{oc,k}$ is the open circuit potential which is a function of $c_{s,k}|_{r_k=R_k}$ fitted from experimental values.

Initial conditions and dimensionless quantities

The DFN model is transient. Consequently, initial conditions at $t = 0$ are given as

$$\begin{aligned} &c_{s,k} = c_{s,k}^0, \qquad k \in \{n,p\} \\ &c_{e,k} = c_{e,k}^0, \qquad k \in \{n,sep,p\} \\ &\phi_{s,k} = \begin{cases} 0, & k = n \\ U_{oc,p}^0 - U_{oc,n}^0, & k = p \end{cases} \qquad k \in \{n,p\} \\ &\phi_{e,k} = -U_{oc,n}^0 \qquad k \in \{n,sep,p\} \\ &U_{oc,k} = U_{oc,k}^0 \qquad k \in \{n,p\} \end{aligned} \tag{A.18}$$

The other quantities are initially set to zero. The equations are implemented in a dimensionless form where a dimensionless quantity a is denoted $\tilde{a}$. The parameters are non-dimensionalized considering the geometry of the cell, discharge timescale, diffusion timescale, and reaction timescale following the methodology presented in [33]. The dimensionless DFN model is summarized in Table A.1 where $\mathcal{C}_e$ is the ratio of electrolyte transport timescale to discharge timescale, $\mathcal{C}_k$ is the ratio of solid diffusion timescale to discharge timescale, $\zeta_e = (R_g T/F)/(I_{ref} L/\zeta_{e,ref})$ where subscript ref denotes reference quantities, and $\mathcal{T}_e$ is the ratio of a reference electrolyte concentration to the maximum concentration in a negative particle. More details regarding the DFN model can be found in the literature, see for instance [34–37].

Table A.1
Dimensionless equations of the DFN model.

Description	Governing equation	k
Molar conservation	$\mathcal{C}_k \frac{\partial \tilde{c}_{s,k}}{\partial \tilde{t}} = \frac{1}{\tilde{r}_k^2}\frac{\partial}{\partial \tilde{r}_k}\left(\tilde{r}_k^2 \frac{\partial \tilde{c}_{s,k}}{\partial \tilde{r}_k}\right)$	$\{n,p\}$
	$\epsilon_k \mathcal{C}_e \mathcal{T}_e \frac{\partial \tilde{c}_{e,k}}{\partial \tilde{t}} = -\mathcal{T}_e \frac{\partial \tilde{N}_{e,k}}{\partial \tilde{x}} + \mathcal{C}_e \frac{\partial \tilde{i}_{e,k}}{\partial \tilde{x}}$	$\{n,sep,p\}$
	$\tilde{N}_{e,k} = -\epsilon_k^{bk} \tilde{D}_{e,k} \frac{\partial \tilde{c}_{e,k}}{\partial \tilde{x}} + \frac{t^+ \mathcal{C}_e}{\mathcal{T}_e} \tilde{i}_{e,k}$	$\{n,sep,p\}$
Charge conservation	$\frac{\partial \tilde{i}_{e,k}}{\partial \tilde{x}} = -\frac{\partial \tilde{i}_{s,k}}{\partial \tilde{x}} = \begin{cases} \tilde{J}_k, & k = n,p \\ 0, & k = sep \end{cases}$	$\{n,sep,p\}$
	$\tilde{i}_{e,k} = \epsilon_k^{bk} \hat{\xi}_e \zeta_e \left[-\frac{\partial \tilde{\phi}_{e,k}}{\partial \tilde{x}} + 2(1-t^+)\frac{\partial \log \tilde{c}_{e,k}}{\partial \tilde{x}}\right]$	$\{n,sep,p\}$
	$\tilde{i}_{s,k} = -\tilde{\sigma}_k \frac{\partial \tilde{\phi}_{s,k}}{\partial \tilde{x}}$	$\{n,p\}$
Intercalation kinetic	$\tilde{J}_k = 2\tilde{J}_{k,0} \sinh\left(\frac{\tilde{\eta}_k}{2}\right)$	$\{n,p\}$

Table B.1
Dimensionless equations of the SPM.

Description	Governing equation	k
Molar conservation	$\mathcal{C}_k \frac{\partial \tilde{c}_{s,k}}{\partial \tilde{t}} = \frac{1}{\tilde{r}_k^2}\frac{\partial}{\partial \tilde{r}_k}\left(\tilde{r}_k^2 \frac{\partial \tilde{c}_{s,k}}{\partial \tilde{r}_k}\right)$	$\{n,p\}$
	$-\frac{\mathcal{T}_k}{\mathcal{C}_k}\frac{\partial \tilde{c}_{s,k}}{\partial \tilde{r}_k}|_{\tilde{r}_k=1} = \begin{cases} \frac{i_{app}}{\tilde{L}_n \tilde{a}_n} & k = n \\ -\frac{i_{app}}{\tilde{L}_p \tilde{a}_p} & k = p \end{cases}$	$\{n,p\}$

Appendix B. Single particle model equations

The dimensionless equations of the SPM [33,72] are summarized in Table B.1 where $\tilde{a}_k$ is the product of the representative particle radius and surface area per unit volume, and $\mathcal{T}_k = c_{k,max}/c_{n,max}$.

Appendix C. Parameter set for the electrochemical models

The parameter set for the models is given in Table C.1.

Appendix D. Mesh convergence study

We investigate the influence of spatial discretization with the geometry and boundary conditions shown in Fig. 4 and the material properties given in Table 1. The volumetric heat generation over the landing segment predicted by the DFN model is used. The volumetric heat generation over the entire flight is shown in Fig. 6. The finite element model is discretized with `nelx` x `nely` x `nelz` hexahedral finite elements where `nelx`, `nely` and `nelz` are the number of finite elements in the x-direction, y-direction, and z-direction, respectively. The x–y plane corresponds to the surface where the film boundary condition is applied. We set `nelx` = `nely` and `nelz` = 7/3 `nelx`. We explore a range of values for `nelx`, from 10 to 40 elements, incrementing by 5 elements. Fig. D.1 depicts the obtained maximum temperature and mean temperature against the number of elements in the x-direction.

The relative difference between `nelx` = 30 and `nelx` = 40 in terms of mean temperature and maximum temperature is 1.17% and 0.83%, respectively. Hence, we consider that `nelx` = 30 suffices for a sufficient representation in comparison to the highest resolution (`nelx` = 40). We use the `nelx` = 30 discretization throughout our investigation.

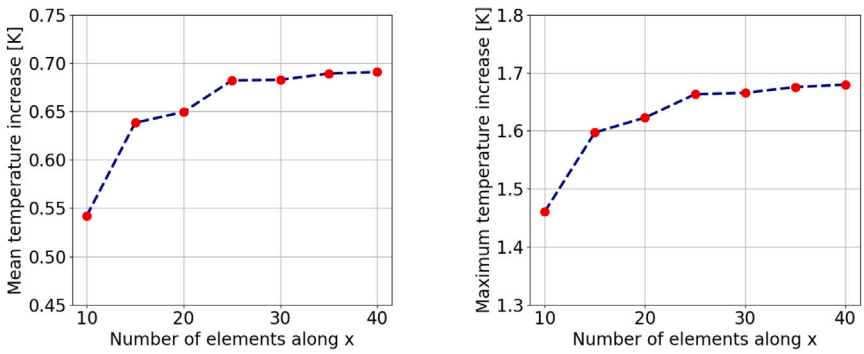

(a) Mean temperature (b) Maximum temperature

Fig. D.1. Mean temperature and maximum temperature as a function of the number of elements in the x-direction (`nelx`).

Table C.1
Parameters for the electrochemical models of the LG Chem INR21700M50LT cell adapted from Chen et al. [42].

Parameter	Value
Cell	
Negative electrode thickness [m]	8.52×10^{-5}
Separator thickness [m]	1.2×10^{-5}
Positive electrode thickness [m]	7.56×10^{-5}
Nominal cell capacity [A h]	5.0
Cation transference number	0.2594
Reference temperature [K]	298.15
Ambient temperature [K]	298.15
Lower voltage cut-off [V]	2.5
Upper voltage cut-off [V]	4.2
Solid electrolyte interface thickness[a] [m]	1.44×10^{-8}
Solid electrolyte interface resistivity[a] [Ohm m]	19×10^{6}
Negative electrode	
Negative electrode conductivity [S m^{-1}]	215.0
Maximum concentration in negative electrode [mol m^{-3}]	33 133.0
Negative particle diffusivity [m^2 s^{-1}]	3.3×10^{-14}
Negative electrode porosity	0.25
Negative particle radius [m]	5.86×10^{-6}
Negative electrode charge transfer coefficient	0.5
Initial concentration in negative electrode [mol m^{-3}]	29 866.0
Positive electrode	
Positive electrode conductivity [S m^{-1}]	0.18
Maximum concentration in positive electrode [mol m^{-3}]	63 104.0
Positive particle diffusivity [m^2 s^{-1}]	4×10^{-15}
Positive electrode porosity	0.335
Positive particle radius [m]	5.22×10^{-6}
Positive electrode charge transfer coefficient	0.5
Initial concentration in positive electrode [mol m^{-3}]	17 038.0
Separator and electrolyte	
Separator porosity	0.47
Electrolyte Bruggeman coefficient	1.5
Initial concentration in electrolyte [mol m^{-3}]	1000.0

[a] Adjusted parameters to consider calendar aging.

References

[1] L. Tom, M. Khowja, G. Vakil, C. Gerada, Commercial aircraft electrification—Current state and future scope, Energies 14 (24) (2021) 8381.
[2] P. Wheeler, S. Bozhko, The more electric aircraft: Technology and challenges, IEEE Electrif. Mag. 2 (4) (2014) 6–12.
[3] I.C. Kleinbekman, M.A. Mitici, P. Wei, eVTOL arrival sequencing and scheduling for on-demand urban air mobility, in: 2018 IEEE/AIAA 37th Digital Avionics Systems Conference, DASC, IEEE, 2018, pp. 1–7.
[4] X.-G. Yang, T. Liu, S. Ge, E. Rountree, C.-Y. Wang, Challenges and key requirements of batteries for electric vertical takeoff and landing aircraft, Joule 5 (7) (2021) 1644–1659.
[5] D.R. Vieira, D. Silva, A. Bravo, Electric VTOL aircraft: the future of urban air mobility (background, advantages and challenges), Int. J. Sustain. Aviat. 5 (2) (2019) 101–118.
[6] L. Baggetto, R.A. Niessen, F. Roozeboom, P.H. Notten, High energy density all-solid-state batteries: a challenging concept towards 3D integration, Adv. Funct. Mater. 18 (7) (2008) 1057–1066.
[7] Y.-p. Liu, C.-z. Ouyang, Q.-b. Jiang, B. Liang, Design and parametric optimization of thermal management of lithium-ion battery module with reciprocating air-flow, J. Cent. South Univ. 22 (10) (2015) 3970–3976.
[8] L. Zhu, F. Xiong, H. Chen, D. Wei, G. Li, C. Ouyang, Thermal analysis and optimization of an EV battery pack for real applications, Int. J. Heat Mass Transfer 163 (2020) 120384.
[9] K. Chen, S. Wang, M. Song, L. Chen, Configuration optimization of battery pack in parallel air-cooled battery thermal management system using an optimization strategy, Appl. Therm. Eng. 123 (2017) 177–186.
[10] W. Li, M. Xiao, X. Peng, A. Garg, L. Gao, A surrogate thermal modeling and parametric optimization of battery pack with air cooling for EVs, Appl. Therm. Eng. 147 (2019) 90–100.
[11] Z. An, K. Shah, L. Jia, Y. Ma, A parametric study for optimization of minichannel based battery thermal management system, Appl. Therm. Eng. 154 (2019) 593–601.
[12] Z. Lu, X. Yu, L. Wei, Y. Qiu, L. Zhang, X. Meng, L. Jin, Parametric study of forced air cooling strategy for lithium-ion battery pack with staggered arrangement, Appl. Therm. Eng. 136 (2018) 28–40.
[13] L. Shui, F. Chen, A. Garg, X. Peng, N. Bao, J. Zhang, Design optimization of battery pack enclosure for electric vehicle, Struct. Multidiscip. Optim. 58 (2018) 331–347.
[14] M.P. Bendsøe, N. Kikuchi, Generating optimal topologies in structural design using a homogenization method, Comput. Methods Appl. Mech. Engrg. 71 (2) (1988) 197–224.
[15] O. Sigmund, K. Maute, Topology optimization approaches, Struct. Multidiscip. Optim. 48 (6) (2013) 1031–1055.
[16] J. Wu, O. Sigmund, J.P. Groen, Topology optimization of multi-scale structures: a review, Struct. Multidiscip. Optim. 63 (2021) 1455–1480.
[17] N.P. Van Dijk, K. Maute, M. Langelaar, F. Van Keulen, Level-set methods for structural topology optimization: a review, Struct. Multidiscip. Optim. 48 (2013) 437–472.
[18] T. Dbouk, A review about the engineering design of optimal heat transfer systems using topology optimization, Appl. Therm. Eng. 112 (2017) 841–854.
[19] T.E. Bruns, Topology optimization of convection-dominated, steady-state heat transfer problems, Int. J. Heat Mass Transfer 50 (15–16) (2007) 2859–2873.
[20] F. Chen, J. Wang, X. Yang, Topology optimization design and numerical analysis on cold plates for lithium-ion battery thermal management, Int. J. Heat Mass Transfer 183 (2022) 122087.
[21] X. Mo, H. Zhi, Y. Xiao, H. Hua, L. He, Topology optimization of cooling plates for battery thermal management, Int. J. Heat Mass Transfer 178 (2021) 121612.
[22] J. Wang, F. Chen, Z. Shao, L. He, Study of the influence of objective functions on the topology optimization design of battery cold plate, Appl. Therm. Eng. 226 (2023) 120326.
[23] C. Guo, H.-l. Liu, Q. Guo, X.-d. Shao, M.-l. Zhu, Investigations on a novel cold plate achieved by topology optimization for lithium-ion batteries, Energy 261 (2022) 125097.
[24] Q. Zhong, P.K. Chandra, W. Li, L. Gao, A. Garg, S. Lv, K. Tai, A comprehensive numerical study based on topology optimization for cooling plates thermal design of battery packs, Appl. Therm. Eng. 236 (2024) 121918.
[25] Z. Mao, S. Yan, Design and analysis of the thermal-stress coupled topology optimization of the battery rack in an AUV, Ocean Eng. 148 (2018) 401–411.
[26] V. Wanittansirichok, K. Mongkholphan, N. Chaowalitbumrung, Y. Sukjai, P. Promoppatum, Topology optimization for liquid-based battery thermal management system under varied charge rates, J. Energy Storage 55 (2022) 105703.

[27] D. Huang, S. Zhou, X. Yan, Multi-objective optimization design of power pack structures based on floating projection topology optimization, Eng. Optim. (2024) 1–23.

[28] S. Kambampati, J.S. Gray, H.A. Kim, Level set topology optimization of structures under stress and temperature constraints, Comput. Struct. 235 (2020) 106265.

[29] S. Kambampati, J.S. Gray, H.A. Kim, Level set topology optimization of load carrying battery packs, Int. J. Heat Mass Transfer 177 (2021) 121570.

[30] M. Doyle, T.F. Fuller, J. Newman, Modeling of galvanostatic charge and discharge of the lithium/polymer/insertion cell, J. Electrochem. Soc. 140 (6) (1993) 1526–1533, http://dx.doi.org/10.1149/1.2221597.

[31] J. Newman, K.E. Thomas-Alyea, Electrochemical Systems, John Wiley & Sons, Hoboken, 2012.

[32] J.S. Newman, C.W. Tobias, Theoretical analysis of current distribution in porous electrodes, J. Electrochem. Soc. 109 (12) (1962) 1183, http://dx.doi.org/10.1149/1.2425269.

[33] S.G. Marquis, V. Sulzer, R. Timms, C.P. Please, S.J. Chapman, An asymptotic derivation of a single particle model with electrolyte, 2019, arXiv:1905.12553.

[34] F. Brosa Planella, M. Sheikh, W.D. Widanage, Systematic derivation and validation of a reduced thermal-electrochemical model for lithium-ion batteries using asymptotic methods, Electrochim. Acta 388 (2021) 138524, http://dx.doi.org/10.1016/j.electacta.2021.138524, arXiv:2011.01611.

[35] R. Timms, S.G. Marquis, V. Sulzer, C. Please, S.J. Chapman, Asymptotic reduction of a lithium-ion pouch cell model, 2020, arXiv:2005.05127.

[36] S.G. Marquis, R. Timms, V. Sulzer, C.P. Please, S.J. Chapman, A suite of reduced-order models of a single-layer lithium-ion pouch cell, J. Electrochem. Soc. 167 (14) (2020) 140513.

[37] T.L. Kirk, C.P. Please, S.J. Chapman, Physical modelling of the slow voltage relaxation phenomenon in lithium-ion batteries, J. Electrochem. Soc. 168 (6) (2021) 060554.

[38] R. Eymard, T. Gallouët, R. Herbin, Finite volume methods, in: Solution of Equation in ℝN (Part 3), Techniques of Scientific Computing (Part 3), in: Handbook of Numerical Analysis, vol. 7, Elsevier, Amsterdam, 2000, pp. 713–1018, http://dx.doi.org/10.1016/S1570-8659(00)07005-8.

[39] V. Sulzer, S.G. Marquis, R. Timms, M. Robinson, S.J. Chapman, Python Battery Mathematical Modelling (PyBaMM), J. Open Res. Softw. 9 (1) (2021) 14, http://dx.doi.org/10.5334/jors.309.

[40] M. Steinhardt, E.I. Gillich, A. Rheinfeld, L. Kraft, M. Spielbauer, O. Bohlen, A. Jossen, Low-effort determination of heat capacity and thermal conductivity for cylindrical 18650 and 21700 lithium-ion cells, J. Energy Storage 42 (2021) 103065.

[41] T. Waldmann, R.-G. Scurtu, K. Richter, M. Wohlfahrt-Mehrens, 18650 Vs. 21700 Li-ion cells–A direct comparison of electrochemical, thermal, and geometrical properties, J. Power Sources 472 (2020) 228614.

[42] C.-H. Chen, F.B. Planella, K. O'regan, D. Gastol, W.D. Widanage, E. Kendrick, Development of experimental techniques for parameterization of multi-scale lithium-ion battery models, J. Electrochem. Soc. 167 (8) (2020) 080534.

[43] T.J.R. Hughes, The Finite Element Method: Linear Static and Dynamic Finite Element Analysis, Dover Publications, New York, 2000.

[44] A. Logg, K.-A. Mardal, G.N. Wells (Eds.), Automated Solution of Differential Equations by the Finite Element Method, in: Lecture Notes in Computational Science and Engineering, vol. 84, Springer, Berlin, 2012, http://dx.doi.org/10.1007/978-3-642-23099-8.

[45] M. Alnæs, J. Blechta, J. Hake, A. Johansson, B. Kehlet, A. Logg, C. Richardson, J. Ring, M. Rognes, G. Wells, The FEniCS project version 1.5, 2015, http://dx.doi.org/10.11588/ans.2015.100.20553, 3.

[46] S. Osher, J.A. Sethian, Fronts propagating with curvature-dependent speed: Algorithms based on Hamilton-Jacobi formulations, J. Comput. Phys. 79 (1) (1988-11) 12–49, http://dx.doi.org/10.1016/0021-9991(88)90002-2.

[47] G. Allaire, F. Jouve, A.-M. Toader, Structural optimization using sensitivity analysis and a level-set method, J. Comput. Phys. 194 (1) (2004) 363–393.

[48] M.Y. Wang, X. Wang, D. Guo, A level set method for structural topology optimization, Comput. Methods Appl. Mech. Engrg. 192 (1–2) (2003) 227–246.

[49] P.D. Dunning, H.A. Kim, Introducing the sequential linear programming level-set method for topology optimization, Struct. Multidiscip. Optim. 51 (3) (2015) 631–643.

[50] R. Sivapuram, P.D. Dunning, H.A. Kim, Simultaneous material and structural optimization by multiscale topology optimization, Struct. Multidiscip. Optim. 54 (2016) 1267–1281.

[51] X.-D. Liu, S. Osher, T. Chan, Weighted essentially non-oscillatory schemes, J. Comput. Phys. 115 (1) (1994) 200–212.

[52] X. Feng, M. Ouyang, X. Liu, L. Lu, Y. Xia, X. He, Thermal runaway mechanism of lithium ion battery for electric vehicles: A review, Energy Storage Mater. 10 (2018) 246–267.

[53] Q. Wang, P. Ping, X. Zhao, G. Chu, J. Sun, C. Chen, Thermal runaway caused fire and explosion of lithium ion battery, J. Power Sources 208 (2012) 210–224.

[54] X. Feng, D. Ren, X. He, M. Ouyang, Mitigating thermal runaway of lithium-ion batteries, Joule 4 (4) (2020) 743–770.

[55] J. Hong, Z. Wang, C. Qu, Y. Zhou, T. Shan, J. Zhang, Y. Hou, Investigation on overcharge-caused thermal runaway of lithium-ion batteries in real-world electric vehicles, Appl. Energy 321 (2022) 119229.

[56] S. Shahid, M. Agelin-Chaab, A review of thermal runaway prevention and mitigation strategies for lithium-ion batteries, Energy Convers. Manag.: X (2022) 100310.

[57] X. Qu, N. Pagaldipti, R. Fleury, J. Saiki, Thermal topology optimization in optistruct software, in: 17th AIAA/ISSMO Multidisciplinary Analysis and Optimization Conference, 2016, p. 3829.

[58] K. Long, X. Wang, X. Gu, Multi-material topology optimization for the transient heat conduction problem using a sequential quadratic programming algorithm, Eng. Optim. 50 (12) (2018) 2091–2107.

[59] C. Silva, W.R. Johnson, E. Solis, M.D. Patterson, K.R. Antcliff, VTOL urban air mobility concept vehicles for technology development, in: 2018 Aviation Technology, Integration, and Operations Conference, 2018, p. 3847.

[60] M.M. Thackeray, C. Wolverton, E.D. Isaacs, Electrical energy storage for transportation—approaching the limits of, and going beyond, lithium-ion batteries, Energy Environ. Sci. 5 (7) (2012) 7854–7863.

[61] M. Fischer, M. Werber, P.V. Schwartz, Batteries: Higher energy density than gasoline? Energy Policy 37 (7) (2009) 2639–2641.

[62] S.K. Mitusch, S.W. Funke, J.S. Dokken, dolfin-adjoint 2018.1: automated adjoints for FEniCS and Firedrake, J. Open Source Softw. 4 (38) (2019) 1292.

[63] S. Kambampati, C. Jauregui, K. Museth, H.A. Kim, Geometry design using function representation on a sparse hierarchical data structure, Comput. Aided Des. 133 (2021) 102989.

[64] L. Sheng, Z. Zhang, L. Su, H. Zhang, H. Zhang, Y. Fang, K. Li, W. Ye, Quasi steady state method to measure thermophysical parameters of cylindrical lithium ion batteries, J. Power Sources 485 (2021) 229342.

[65] M. Steinhardt, J.V. Barreras, H. Ruan, B. Wu, G.J. Offer, A. Jossen, Meta-analysis of experimental results for heat capacity and thermal conductivity in lithium-ion batteries: A critical review, J. Power Sources 522 (2022) 230829.

[66] P.T. Coman, E.C. Darcy, C.T. Veje, R.E. White, Numerical analysis of heat propagation in a battery pack using a novel technology for triggering thermal runaway, Appl. Energy 203 (2017) 189–200.

[67] E. Darcy, Passively thermal runaway propagation resistant battery module that achieves> 190 Wh/kg, in: Sustainable Aviation Symposium, 2016.

[68] P.H. Camargos, P.H. dos Santos, I.R. dos Santos, G.S. Ribeiro, R.E. Caetano, Perspectives on Li-ion battery categories for electric vehicle applications: a review of state of the art, Int. J. Energy Res. 46 (13) (2022) 19258–19268.

[69] M. Armand, P. Axmann, D. Bresser, M. Copley, K. Edström, C. Ekberg, D. Guyomard, B. Lestriez, P. Novák, M. Petranikova, et al., Lithium-ion batteries–Current state of the art and anticipated developments, J. Power Sources 479 (2020) 228708.

[70] S. Pelletier, O. Jabali, G. Laporte, M. Veneroni, Battery degradation and behaviour for electric vehicles: Review and numerical analyses of several models, Transp. Res. B 103 (2017) 158–187.

[71] X. Han, L. Lu, Y. Zheng, X. Feng, Z. Li, J. Li, M. Ouyang, A review on the key issues of the lithium ion battery degradation among the whole life cycle, ETransportation 1 (2019) 100005.

[72] F. Brosa Planella, W. Ai, A.M. Boyce, A. Ghosh, I. Korotkin, S. Sahu, V. Sulzer, R. Timms, T.G. Tranter, M. Zyskin, et al., A continuum of physics-based lithium-ion battery models reviewed, Prog. Energy 4 (4) (2022) 042003.